Electronic Supplementary Information for:

Counterion Influence on Dynamic Spin Properties in a V(IV) Complex

Chun-Yi Lin,[1] Thacien Ngendahimana,[2] Gareth R. Eaton,*[2] Sandra S. Eaton,*[2] and Joseph M. Zadrozny*[1]

[1] *Department of Chemistry, Colorado State University, Fort Collins, Colorado 80523, USA.*

[2] *Department of Chemistry and Biochemistry, University of Denver, Denver, Colorado 80208, USA.*

Table of Contents

Full Experimental Details

General Considerations. The complex $(Et_3NH)_2[V(C_6H_4O_2)_3]$ (**1**) was reported to be air-sensitive.[1] Thus, all manipulations and syntheses of it and **2**−**4** were performed under a N_2 atmosphere with either a Vigor glovebox or Schlenk techniques. Glassware was either oven-dried at 150 °C for at least 4 h and/or flame-dried before bringing into the glovebox. Acetonitrile (CH_3CN), tetrahydrofuran (THF), diethyl ether (Et_2O), and hexanes were dried using a commercial solvent purification system from LC Technology Solutions and were stored over 3 or 4 Å molecular sieves prior to use. 3 or 4 Å molecular sieves were stored in a 150 °C oven and were activated at 280 °C under reduced pressure for at least 12 h prior to use. THF, Et_2O, and hexanes were subjected to a test with a standard purple solution of sodium benzophenone ketyl in THF to confirm low O_2 and H_2O content. Triethylamine (Et_3N), tri-*n*-butylamine (*n*-Bu_3N), tri-*n*-hexylamine (*n*-Hex_3N), tri-*n*-octylamine (*n*-Oct_3N), and hexamethyldisiloxane (HMDSO) were purchased from commercial suppliers and dried by stirring for at least 24 h then distilled over CaH_2. Catechol was purchased from commercial suppliers and was purified by published procedure.[2] *o*-Terphenyl was purchased from commercial suppliers and was used as received. Vanadyl acetylacetonate, $VO(acac)_2$,[3] and $(Et_3NH)_2[V(C_6H_4O_2)_3]$ (**1**)[1,4] were prepared following the literature procedures.

(*n*-$Bu_3NH)_2[V(C_6H_4O_2)_3]$ (2) In a N_2-filled glovebox, a 20-mL scintillation vial was charged with 0.255 g (0.962 mmol) $VO(acac)_2$, 0.322 g (2.92 mmol) catechol, and a Teflon-coated magnetic stir bar. A solution containing 0.417 g (2.25 mmol) *n*-Bu_3N in 5 mL THF was added to the mixture with gentle shaking, resulting almost immediately in an intensely dark blue solution. The reaction mixture was allowed to stir overnight. All volatile materials (THF, H_2O, and acetylacetone) were removed under reduced pressure. The resulting dark blue residue was washed twice with ca. 5 mL cold Et_2O (Note: the complex is slightly soluble in Et_2O) and twice with ca. 5 mL hexanes and then was dried under reduced pressure to yield 0.50 g of dark blue powder. The solid was further purified by crystallization with hexanes/THF in a −35 °C freezer in the glovebox for 2−3 days to afford 0.485 g (0.648 mmol, 67.4 % yield) of large, shiny, dark blue crystals suitable for single-crystal X-ray diffraction (See Figure S22 for picture). Note: THF found in the crystal

structure can be removed by heating crushed crystals at 50 °C under reduced pressure for 1−2 h. The ^{1}H NMR spectrum of **2** in $CDCl_3$ reveals extremely broadened signals that are depicted in Fig. S2. IR (KBr, cm^{-1}): 3048, 2956, 2872, 1568, 1465, 1377, 1253, 1097, 1014, 870, 799, 733, 628, 537, 501, 412. UV-vis (CH_3CN); λ_{max} (ε_M, $M^{-1}cm^{-1}$): 289 (17000), 347 (5000), 559 (8000), 658 (7100). LTQ-MS (m/z): positive ion mode: {*n*-Bu_3NH}$^+$, 186.25 (base); {(*n*-$Bu_3NH)_2[V(C_6H_4O_2)_3]$}$^+$, 748.46; negative ion mode: {$H[V(C_6H_4O_2)_3]$}$^-$, 376.08. Combustion analyses calculated for $C_{42}H_{68}N_2O_6V$ (found): 67.45 (67.25) % C; 9.16 (9.08) % H; 3.75 (3.68) % N.

(*n*-$Hex_3NH)_2[V(C_6H_4O_2)_3]$ (3) In a N_2-filled glovebox, a 20-mL scintillation vial was charged with 0.245 g (0.924 mmol) $VO(acac)_2$, 0.307 g (2.79 mmol) catechol, and a Teflon-coated magnetic stir bar. Solution containing 0.587 g (2.18 mmol) *n*-Hex_3N in 5 mL THF was added to the mixture was added to the mixture with gentle shaking, resulting in a very dark blue solution almost immediately. The reaction mixture was allowed to stir overnight. All volatile materials (THF, H_2O, and acetylacetone) were removed under reduced pressure. The resulting dark blue residue was washed twice with ca. 5 mL cold Et_2O (Note: the complex is slightly soluble in Et_2O) and twice with ca. 5 mL hexanes and then was dried under reduced pressure to yield 0.80 g of a very dark blue powder. The solid was further purified by recrystallization with hexanes/THF in a −35 °C freezer in the glovebox for 2−3 days to afford 0.780 g (0.851 mmol, 92.2 % yield) of large, shiny, dark blue crystals suitable for single-crystal X-ray diffraction (See Figure S22 for picture). The ^{1}H NMR spectrum of **3** in $CDCl_3$ reveals extremely broadened signals that are depicted in Fig. S3. IR (KBr, cm^{-1}): 3064, 2957, 2856, 1569, 1466, 1372, 1253, 1100, 1018, 892, 869, 803, 727, 626, 538, 498, 412. UV-vis (CH_3CN); λ_{max} (ε_M, $M^{-1}cm^{-1}$): 289 (18000), 350 (5000), 560 (8000), 657 (7200). LTQ-MS (m/z): positive ion mode: {*n*-Hex_3NH}$^+$, 270.42 (base); {(*n*-$Hex_3NH)_2[V(C_6H_4O_2)_3]$}$^+$, 916.50; negative ion mode: {$H[V(C_6H_4O_2)_3]$}$^-$, 376.16. Combustion analyses calculated for $C_{54}H_{92}N_2O_6V$ (found): 70.79 (71.01) % C; 10.12 (10.17) % H; 3.06 (2.88) % N.

(*n*-$Oct_3NH)_2[V(C_6H_4O_2)_3]$ (4) In a N_2-filled glovebox, a 100-mL Schlenk flask was charged with 0.204 g (0.769 mmol) $VO(acac)_2$, 0.293 g (2.66 mmol) catechol and a Teflon-coated magnetic stir bar. Solution

containing 0.711 g (2.01 mmol) *n*-Oct_3N in 10 mL THF was added to the mixture was added to the mixture with gentle shaking, resulting in a very dark blue solution almost immediately. The flask was capped and taken outside the glovebox and heated with an 80 °C oil bath for 12 h (Note: the heating step is crucial in obtaining pure product). All volatile materials (THF, H_2O, and acetylacetone) were removed under reduced pressure. After the mixture was visibly dry, the flask was heated to 80 °C under reduced pressure for 2 h. The resulting dark blue oil was washed three times with ca. 5 mL HMDSO to remove excess *n*-Oct_3N and then was dried under reduced pressure to yield dark blue oil. The oil was dissolved in Et_2O, layered with hexanes, and was put in a −35 °C freezer in the glovebox for 2−3 days to afford 0.485 g (0.447 mmol, 58.1 % yield) of dark blue oil (See Figure S22 for picture). The ^1H NMR spectrum of **4** in $CDCl_3$ reveals extremely broadened signals that are depicted in Fig. S4. IR (KBr, cm^{-1}): 3055, 2957, 2927, 2855, 1572, 1466, 1376, 1254, 1098, 1018, 870, 802, 730, 631, 537, 502, 415. UV-vis (CH_3CN); λ_{max} (ε_M, $M^{-1}cm^{-1}$): 289 (18000), 355 (4900), 559 (7900), 656 (7100). LTQ-MS (m/z): positive ion mode: $\{n\text{-}Oct_3NH\}^+$, 354.58 (base); $\{(n\text{-}Oct_3NH)_2[V(C_6H_4O_2)_3]\}^+$, 1083.67; negative ion mode: $\{H[V(C_6H_4O_2)_3]\}^-$, 376.16. Combustion analyses calculated for $C_{66}H_{116}N_2O_6V$ (found): 73.09 (72.80) % C; 10.78 (11.02) % H; 2.58 (2.27) % N.

X-Ray Data Collection, Structure Solution and Refinement for 2•$(THF)_2$ and 3. The diffraction data were collected at the X-Ray Diffraction facility of the Central Instrument Facility at Colorado State University. Data for **2•$(THF)_2$** were collected on a Bruker D8 Quest ECO single-crystal X-ray diffractometer equipped with Mo Kα (λ = 0.71073 Å) radiation, whereas data for **3** were collected on a Bruker APEX II diffractometer with Mo Kα radiation. Data were collected and integrated using Bruker Apex 3 software. Absorption correction were applied using SADABS.[5] Space group assignments were determined by examination of systematic absences, E-statistics, and successive refinement of the structures. Crystal structures were solved using SHELXT and refined with the aid of successive difference Fourier maps by SHELXL operated in conjunction with OLEX2 software.[6–8] None of the crystals demonstrated decay by X-ray radiation over the course of the experiment. Hydrogen atoms were placed in ideal positions

and refined using a riding model for all structures. In **2•(THF)$_2$**, the cocrystallized THF molecule is partially disordered over two positions and were modeled using free variables, yielding occupancies of 0.629(9) and 0.371(9). In **3**, one of the catecholate ligands is positionally disordered over two positions and were modeled using free variables, yielding occupancies of 0.64(1) and 0.36(1). One of the alkyl chains of the tri-*n*-hexylammonium ion was also partially disordered over two positions, and they were modeled freely, resulting in occupancies of 0.74(2) and 0.26(2). See Tables S1 and S2 for refinement details.

Electron Paramagnetic Resonance. EPR spectra collected herein were simulated using Easyspin[9] with the function pepper (frozen solution and solid) or garlic (fluid solution), and were refined using the function esfit. Samples were prepared under an inert atmosphere. Samples for room-temperature (ca. 290 K) solid-state EPR spectra of **1**−**4** were prepared by loading powdered **1**−**3** and liquid **4** or 10 mM solution (CH_3CN, THF, and toluene) of **1**−**4** (except **1** in toluene owing to its insolubility) into a 4 mm outer diameter (OD) quartz EPR tube (Wilmad 707-SQ-250M) in a glove box, sealed with a septum, and collected immediately on a Bruker ESR-300 spectrometer (Bruker Biospin, Rheinstetten, Germany). Samples for pulsed EPR studies were prepared by first loading 0.1 mL 1 mM THF solution into a 4 mm OD quartz EPR tube. Following removal of THF under reduced pressure, 0.116 g *o*-terphenyl (0.1 mL when molten) was loaded into the same tube. These tubes were flame sealed under dynamic vacuum (< 50 mTorr) and placed in a 65−70 °C oil bath until a clear dark blue solution formed. These samples were then frozen in liquid N_2 for measurement. While sample tubes prepared in this manner can be stored at room temperature for an extended period without compound decomposition, the quality of glass appeared to decay with extended time on the basis of spectral quality (see Fig. S23). Hence, prior to each measurement, the samples were remelted and frozen.

All pulsed EPR data were collected at the University of Denver EPR Center[10] (Denver, CO, USA) on a Bruker E580 X-Band spectrometer equipped with an ER4118X-MS5 split ring resonator, an Oxford CF935 liquid helium cryostat, and an Oxford ITC503 temperature controller for cryogenic temperatures. The microwave frequency was in the range 9.3−9.4 GHz. Sample tubes were gently melted using a heat

gun to afford a homogeneous dark blue solution, then quickly inserted into the precooled resonator to ensure glassing behavior (the glass transition temperature of *o*-terphenyl is ca. −30 °C). Echo-detected, field-swept (EDFS) spectra were constantly collected and checked for glassing behavior throughout the measurement (see Fig. S22 for a comparison of the EDFS spectra of a glass sample and a non-glass sample). In all cases, the resonator was overcoupled to a Q of ca. 100 to minimize ringdown following application of the microwave pulses. The data collected were processed using Xepr, Matlab 2018a, and Origin Pro 2018b software packages.[11,12]

T_1 data were collected on the most intense resonance (3200−3300 G, the transition of ($|M_S,M_I\rangle$) $|-1/2, +3/2\rangle \rightarrow |+1/2,+3/2\rangle$ in the EDFS spectra via an inversion recovery sequence ($\pi - T - \pi/2 - \tau - \pi - \tau -$ echo) with an 8-step phase cycle. The length of the three pulses, $\pi - \pi/2 - \pi$, are 32 − 16 − 32 ns with a starting T value of 360 ns and τ of 120 ns. The inversion recovery data, except 100 mM **3** in *o*-terphenyl, were fit using the following equation,[13]

$$\mathrm{I}(t) = -A\left[e^{-\left(\frac{t}{T_1}+\sqrt{\frac{t}{q}}\right)} - \mathrm{I}(0) - 1\right]$$

Here, q is the spectral diffusion parameter, which is important at low temperatures. We note that a biexponential fit is better than a single exponential fit below 40−50 K, however, the opposite is true at higher temperatures. To avoid the problems of two different regimes, we approached fitting with the above equation, which can successfully fit all recovery curves in our studies, see Fig. 4 and S10−S12 for selected data and fits. We note that q is non-negligible in the temperature range of 5−40 K, indicating the significance of spectral diffusion, an expected observation for inversion recovery experiments.[13,14] For the 100 mM **3** in *o*-terphenyl data, the biexponential fits were better than the spectral diffusion equation (see Fig. S21), indicating two distinct relaxation processes, as expected for highly concentrated samples.[15]

The temperature-dependent T_1 data were fit using the following equation performed in Mathcad software:

$$\frac{1}{T_1} = A_{\mathrm{dir}} T + A_{\mathrm{Ram}} \left(\frac{T}{\theta_{\mathrm{D}}}\right)^9 J_8\left(\frac{\theta_{\mathrm{D}}}{T}\right) + A_{\mathrm{loc}} \left[\frac{e^{\Delta_{\mathrm{loc}}/T}}{\left(e^{\Delta_{\mathrm{loc}}/T} - 1\right)^2}\right]$$

Here, $J_8\left(\frac{\theta_{\mathrm{D}}}{\mathrm{T}}\right)$ is the transport integral:

$$J_8\left(\frac{\theta_{\mathrm{D}}}{T}\right) = \int_0^{\theta_{\mathrm{D}}/T} x^8 \frac{\mathrm{e}^x}{(\mathrm{e}^x - 1)^2}\,\mathrm{d}x$$

Analysis of the temperature dependence of $1/T_1$ in terms of contributions from the direct process, Raman process, and local mode is not amenable to procedures such as simplex minimization of least-squares errors because such processes do not contribute equally in all temperature ranges. Further, in many cases some adjustable parameters are correlated. For vanadium complexes, literature precedent indicates that the direct process dominates at temperatures below about 10 K, the Raman process makes substantial contributions between about 8 and 70 K, and the local mode makes increasingly significant contributions above about 50 K.[16] Note that the coefficient of the Raman process is correlated with the Debye temperature − if the Debye temperature is increased, then the coefficient of the Raman process must be increased to obtain a similar calculated value at a particular temperature. Analogously, the coefficient of the local mode process is correlated with the energy of the local mode. Fit parameters were adjusted manually to decrease systematic dependence of the deviation between calculated and experimental values as a function of temperature and to minimize the root-mean-square deviation. The starting point in the simulations was the Raman process. The Debye temperature and coefficient of the Raman process were adjusted to approximately match data up to about 60 K. The coefficient for the direct process was adjusted to match the points at lowest temperatures. Next, the energy of the local mode and coefficient of the local mode process were adjusted to match data at higher temperatures, which required adjusting the parameters for the Raman process. Parameters were then iterated to find the best overall fit with the data. Uncertainties were estimated by testing the range of values within which each parameter could be varied, with compensation from other parameters, while still maintaining good agreement between the experimental and calculated data.

T_m data were collected on the most intense resonance (3200−3300 G) in the EDFS spectra via a Hahn echo sequence ($\pi/2 - \tau - \pi - \tau -$ echo) with a 4-step phase cycle with microwave pulses of 16 ($\pi/2$) and 32 ns (π) and an interpulse time (τ) of 300 ns. The Hahn echo decay data were fit using the stretched exponential equation:

$$\mathrm{I}(\tau) = I(0) - Ae^{-\left(\frac{2\tau}{T_2}\right)^{\beta}}$$

Here, β is the stretch parameter. The low temperature data were better fit with stretched exponential equation due to the dominant nuclear spin diffusion. We found that β approached 1 as the temperature increased to roughly 70−80 K (Table S9), indicating that a conventional single exponential fit could be used. Nevertheless, we used the stretched exponential fit throughout the whole temperature range for consistency.

Additional EPR Analysis. For the simulation of 5 K frozen *o*-terphenyl spectra, we found that it is very difficult to use a least square fitting method (esfit in Easyspin) to simulate EDFS spectra due to the number of parameters (*g*, *g*-strain, *A*, and *A*-strain). We found that different sets of spin Hamiltonian parameter could simulate the spectra satisfactorily according to the program. For example, the spectra of **1**−**4** in frozen *o*-terphenyl at 5 K could be simulated satisfactorily by either A_z of ca. 60 MHz or 150 MHz. However, due to their similarity of *A* parameters in fluid solution across **1**–**4**, we believe that the A_z should also be similar in frozen solution. Thus, the simulation and obtained parameters were additionally checked and guided by the A_{iso} parameters in the solution phase study.

In fluid solution, the rotationally effective radius (r, assuming that **1**−**4** are of spherical shapes) of the molecule was estimated using Stokes-Einstein equation:[17]

$$r = \sqrt[3]{\frac{3k_B T \tau_c}{4\pi\eta}}$$

Where k_B is the Boltzmann constant (1.38×10^{-23} $m^2 \cdot kg \cdot s^{-2} K^{-1}$), T the temperature in Kelvin, τ_c the correlation time in second, and η is the viscosity of the solvent (toluene, 5.6×10^{-4} $kg \cdot m^{-1} \cdot s^{-1}$; THF, 4.56

$\times 10^{-4}$ kg·m^{-1}·s^{-1}; CH_3CN, 3.69 $\times 10^{-4}$ kg·m^{-1}·s^{-1}).[18] The calculated values of r (in Å) are summarized below:

	1	**2**	**3**	**4**
CH_3CN	6.3	6.8	7.1	7.6
THF	6.8	7.9	8.4	9.0
toluene		8.8	9.1	9.2

Other Physical Measurements. ^{1}H NMR spectra were collected on a Bruker Avance NEO 400 MHz spectrometer. The spectra were referenced using residual protiated solvent signal as an internal standard ($CDCl_3$, 7.26 ppm). Combustion analyses were performed by Midwest Microlab (Indianapolis, IN, USA). Infrared spectra were recorded on a Bruker TENSOR II FTIR spectrometer. Electronic absorption spectra were recorded on acetonitrile solutions of **2**−**4** with a Hewlett-Packard 8453 spectrophotometer using air-free quartz cuvettes with a 1 cm path length. Linear trap quadruple mass spectrometry (LTQ-MS) measurements were performed on acetonitrile solutions of **2**−**4** with a Thermo-Finnigan LTQ LC/MS-MS at the Central Instrument Facility (CIF) of the Colorado State University.

Table S1 Crystallographic information for the structural refinement of **2•(THF)$_2$**.

Empirical formula	$C_{50}H_{84}N_2O_8V$
Formula weight	892.13 g/mol
Temperature	99.93 K
Crystal system	monoclinic
Space group	C2/c
a	12.8268(11) Å
b	21.9164(19) Å
c	17.7812(15) Å
α	90°
β	99.648(3)°
γ	90°
Volume	4927.9(7) Å^3
Z	4
ρ_{calc}	1.202 g/cm^3
μ	0.254 mm^{-1}
F(000)	1940.0
Crystal color	Dark blue
Crystal size	0.403 × 0.202 × 0.184 mm^3
Radiation	MoKα (λ = 0.71073 Å)
2θ range for data collection	5.516 to 51.36°
Index ranges	$-15 \leq h \leq 15$, $-26 \leq k \leq 26$, $-21 \leq l \leq 21$
Reflections collected	34618
Independent reflections	4629 [R_{int} = 0.0553, R_{sigma} = 0.0324]
Data/restraints/parameters	4629/5/280
Goodness-of-fit on F^2	1.229
Final R indexes [I≥2σ (I)]	R_1 = 0.0657, wR_2 = 0.1446
Final R indexes [all data]	R_1 = 0.0756, wR_2 = 0.1510
Largest diff. peak/hole	0.50/−0.38 e·Å^{-3}

Table S2 Crystallographic information for the structural refinement of **3**.

Empirical formula	$C_{54}H_{92}N_2O_6V$
Formula weight	916.23 g/mol
Temperature	100.37 K
Crystal system	monoclinic
Space group	Cc
a	21.013(5) Å
b	23.356(6) Å
c	15.400(3) Å
α	90°
β	132.546(6)°
γ	90°
Volume	5568(2) $Å^3$
Z	4
ρ_{calc}	1.093 g/cm^3
μ	0.224 mm^{-1}
F(000)	2004.0
Crystal color	Dark blue
Crystal size	0.402 × 0.368 × 0.256 mm^3
Radiation	MoKα (λ = 0.71073 Å)
2θ range for data collection	3.488 to 52.744°
Index ranges	$-26 \le h \le 26$, $-29 \le k \le 29$, $-19 \le l \le 19$
Reflections collected	49029
Independent reflections	11209 [R_{int} = 0.0490, R_{sigma} = 0.0496]
Data/restraints/parameters	11209/27/565
Goodness-of-fit on F^2	1.150
Final R indexes [I≥2σ (I)]	R_1 = 0.0696, wR_2 = 0.1624
Final R indexes [all data]	R_1 = 0.0848, wR_2 = 0.1717
Largest diff. peak/hole /	0.54/−1.02 $e \cdot Å^{-3}$
Flack parameter	0.090(10)

Table S3 Selected mean interatomic distances and angles of **1**−**3**.

	1[a]	**2•(THF)$_2$**	**3**
V−O (Å)	1.94(1)	1.94(2)	1.95(2)
O−V−O[b] (°)	81(1)	81.0(3)	81(1)
R_3NH^+•••O[c] (Å)	1.934(3)	1.735(2)	1.734(5)
V•••V[d] (Å)	9.499(3)	10.9312(8)	9.662(2)
V•••C_{methyl} (Å)	4.613(6) 4.633(6) 4.835(6) 5.379(7) 5.562(5) 5.566(5) Avg. 5.1(4)	5.977(4) 6.379(4) 8.828(3) Avg. 7(1)	8.090(7) 8.150(7) 8.272(5) 8.347(5) 9.479(7) 9.483(8) Avg. 8.6(7)

[a]Data from ref. 4. [b]Catecholate ligand bite angle. [c]Hydrogen bonding distance. [d]Closest V•••V distance.

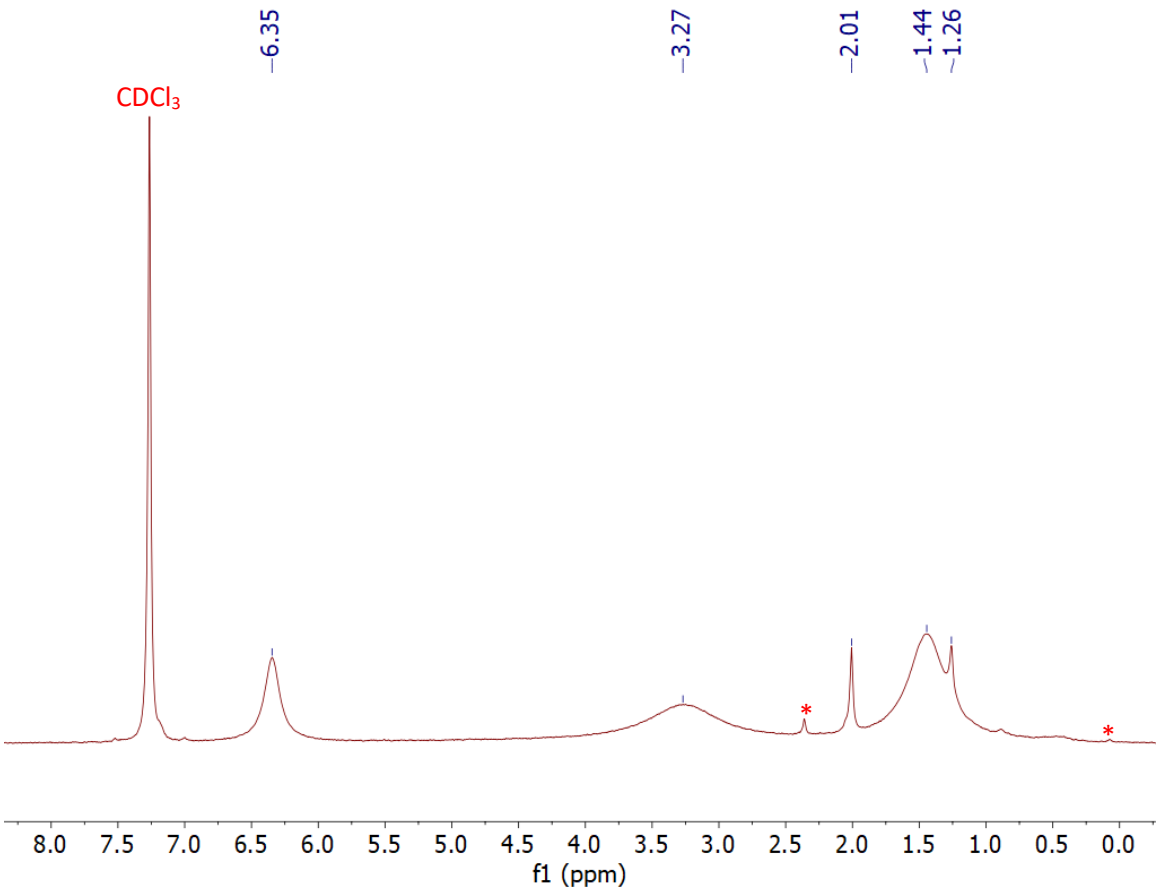

Fig. S1. ^{1}H NMR spectrum of **1** in $CDCl_3$. No signal was observed outside this spectral range. Asterisks denote impurities in the NMR solvent.

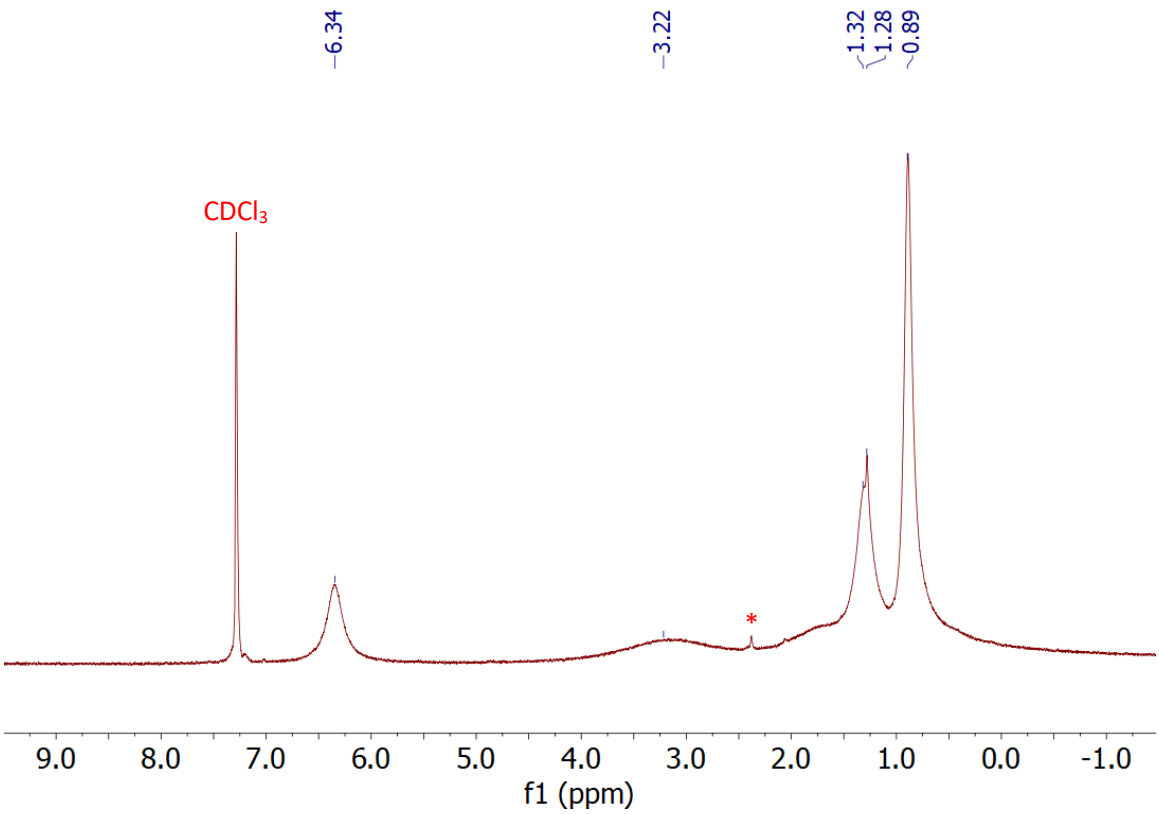

Fig. S2 ^{1}H NMR spectrum of **2** in $CDCl_3$. No signal was observed outside this spectral range. Asterisk denotes impurities in the NMR solvent.

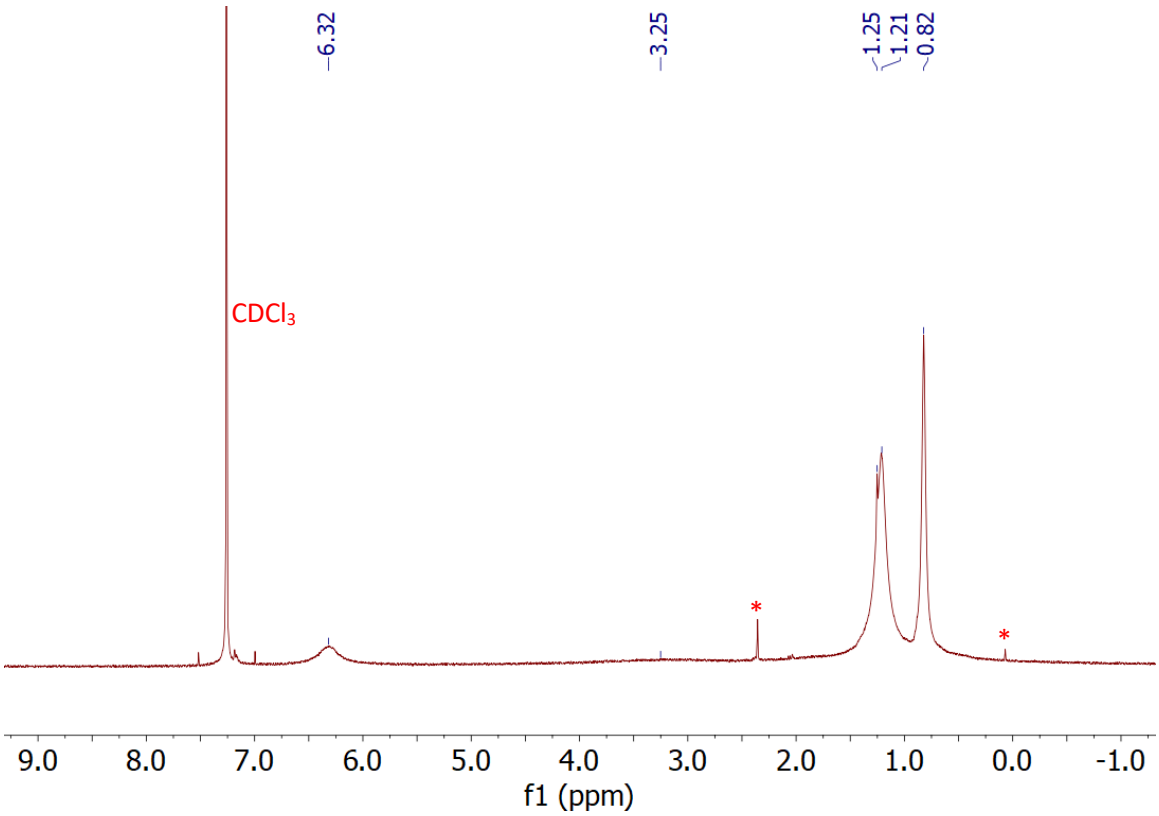

Fig. S3 ^{1}H NMR spectrum of **3** in $CDCl_3$. No signal was observed outside this spectral range. Asterisk denotes impurities in the NMR solvent.

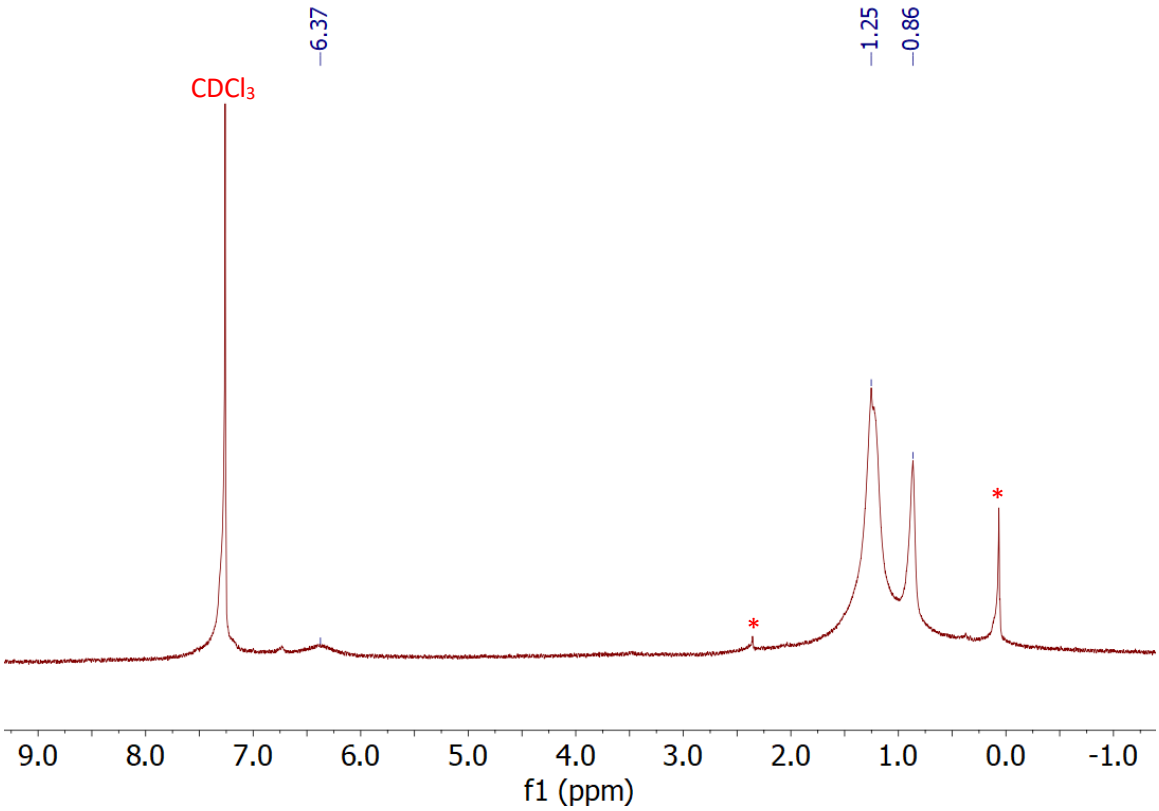

Fig. S4 ^{1}H NMR spectrum of **4** in $CDCl_3$. No signal was observed outside this spectral range. Asterisk denotes impurities in the NMR solvent.

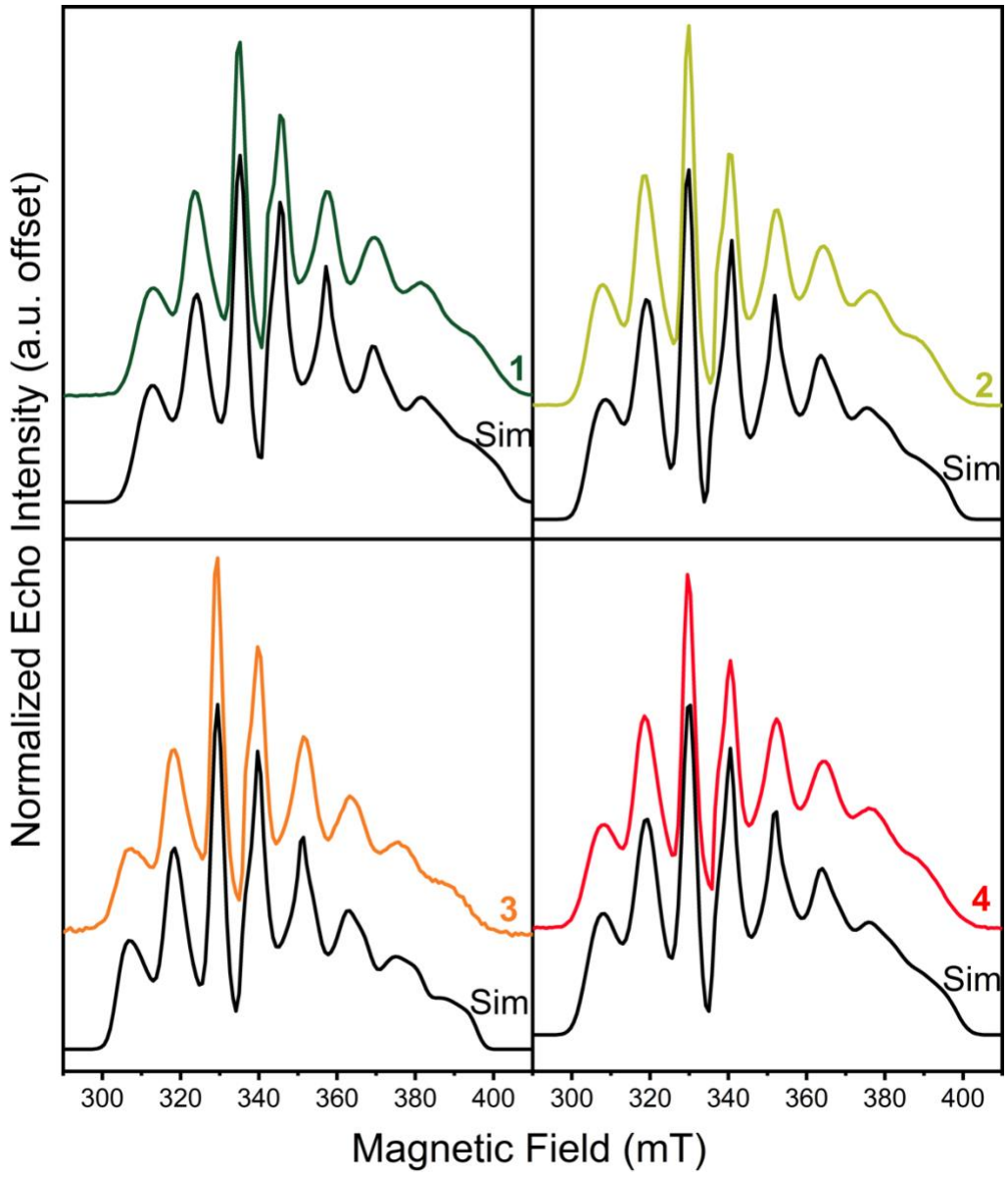

Fig. S5 X-Band echo-detected, field-swept spectra of 1 mM **1**−**4** in *o*-terphenyl solutions at 5 K and simulations (black). Simulated spin Hamiltonian parameters are given in Table S4.

Table S4 EDFS spin Hamiltonian parameters for **1**−**4** in *o*-terphenyl collected at 5 K. The standard errors for these parameters were not available from the simulating process.

Complex	**1**	**2**	**3**	**4**
g_x	1.942	1.935	1.938	1.942
g_y	1.928	1.919	1.922	1.927
g_z	1.991	1.982	1.987	1.992
g_x strain	0[a]	0[a]	0[a]	0[a]
g_y strain	0.032	0.027	0.02	0.034
g_z strain	0[a]	0[a]	0[a]	0[a]
A_x (MHz)	310	313	300	313
A_y (MHz)	367	363	350	368
A_z (MHz)	60	60	52	60
A_x strain (MHz)	49	39	61	44
A_y strain (MHz)	0[a]	0[a]	0[a]	0[a]
A_z strain (MHz)	44	7	60	22

[a] Set as 0 due to consistently low ($< 10^{-5}$) value after several simulations.

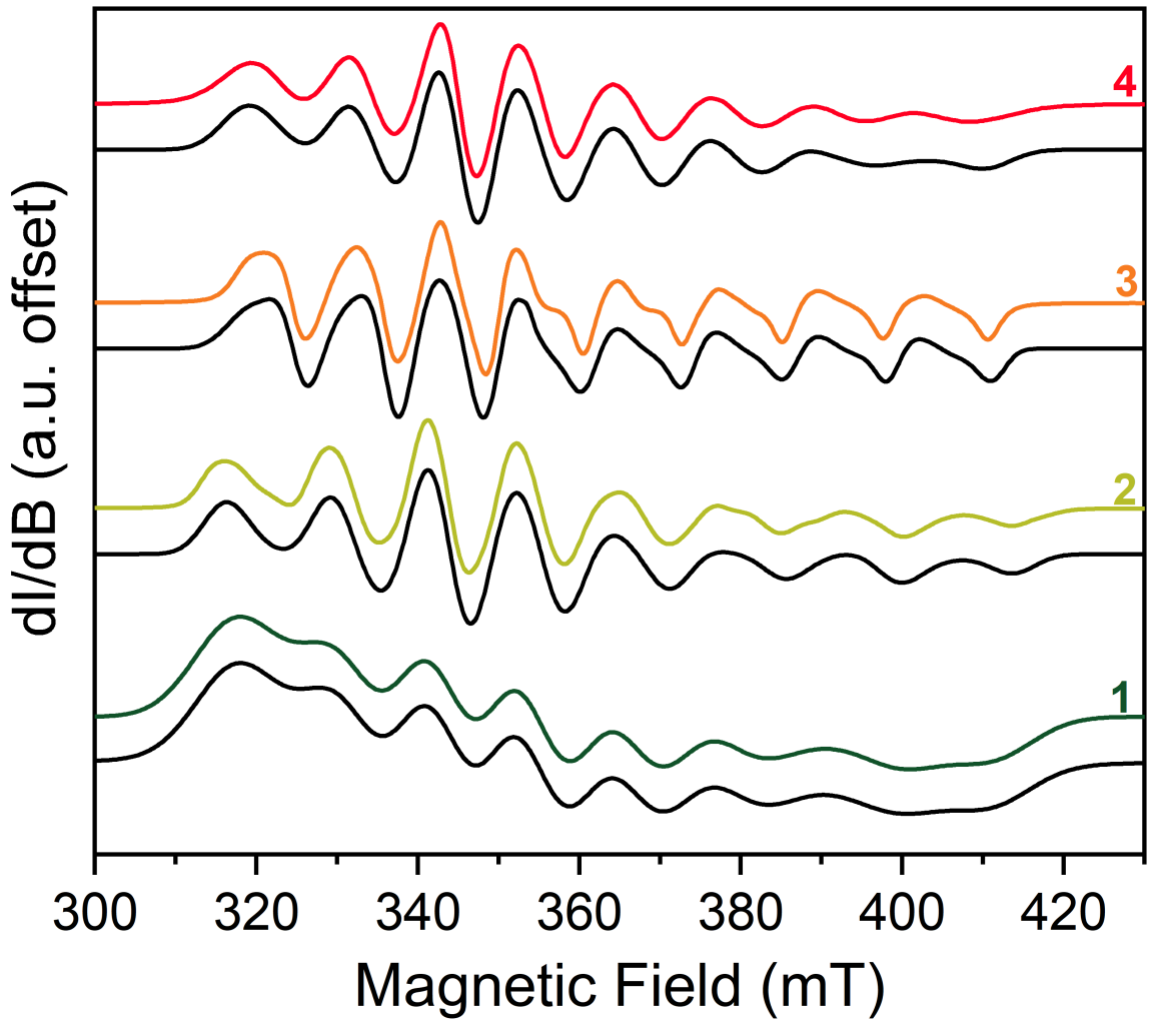

Fig. S6 Stacked X-Band (ca. 9.84 GHz) EPR spectra of solid **1**−**3** and liquid **4** simulations (black). Simulated spin Hamiltonian parameters are given in Table S5.

Table S5 Spin Hamiltonian parameters for powdered **1**−**3** and liquid **4** collected at room temperature (ca. 290 K). The standard errors for these parameters were not available by the simulation process.

Complex	**1**	**2**	**3**	**4**
g_x	1.939	1.942	1.943	1.934
g_y	1.929	1.924	1.910	1.927
g_z	1.986	1.991	1.994	1.988
g_x strain	0.061	0.048	0.036	0.043
g_y strain	0.062	0.034	0.020	0.039
g_z strain	0.070	0.040	0.028	0.024
A_x (MHz)	285	282	332	284
A_y (MHz)	365	374	330	353
A_z (MHz)	24	24	13	30
A_x strain (MHz)	–[a]	0[b]	0[b]	0[b]
A_y strain (MHz)	–[a]	0[b]	4	0[b]
A_z strain (MHz)	–[a]	13	30	14

[a] Not required for satisfactory simulation. [b] Set as 0 due to consistently low ($< 10^{-5}$) value after several simulations.

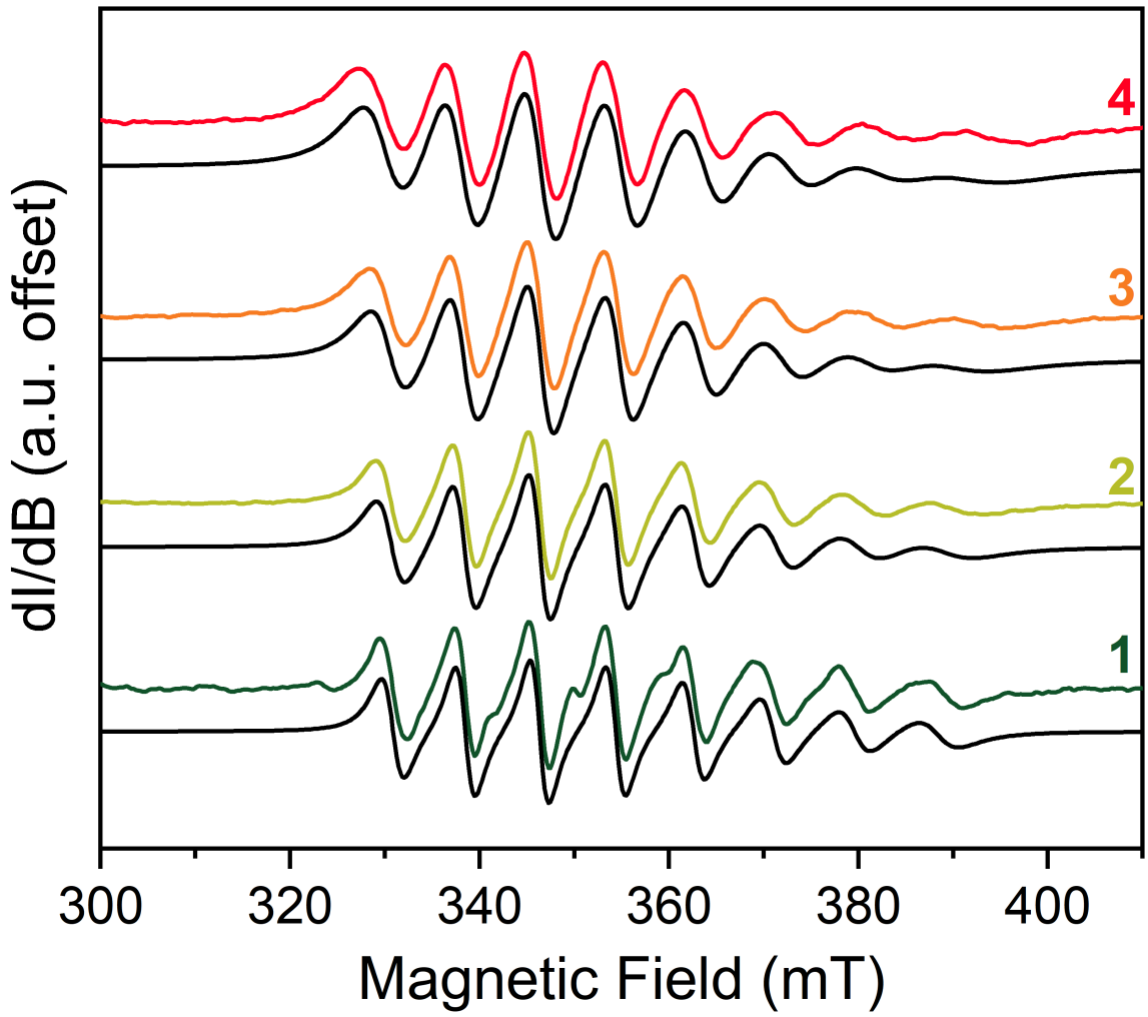

Fig. S7 Stacked X-Band (ca. 9.84 GHz) EPR spectra of **1**−**4** in THF and simulations (black). Simulated spin Hamiltonian parameters are given in Table S6. Experimental details: 10 mM solutions; 0.6325 mW microwave power; microwave frequency, ca. 9.84 GHz; modulation frequency, 100 kHz; modulation amplitude, 1.0 G; number of scans ranged from 16 to 32 to obtain good signal-to-noise ratios.

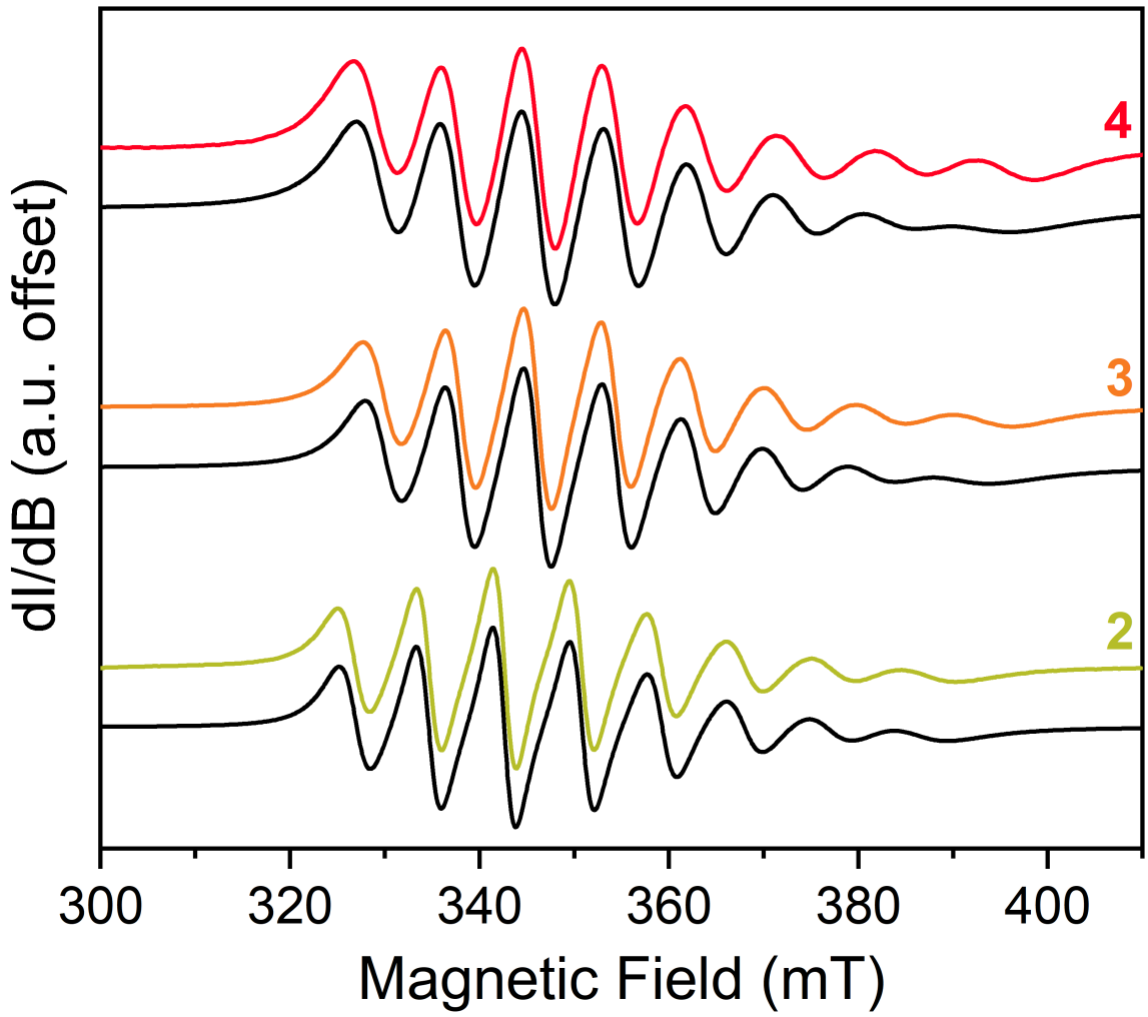

Fig. S8 Stacked X-Band (ca. 9.84 GHz) EPR spectra of **2**−**4** in toluene and simulations (black). Simulated spin Hamiltonian parameters are given in Table S6. Experimental details: 10 mM solutions; 0.6325 mW microwave power; microwave frequency, ca. 9.84 GHz; modulation frequency, 100 kHz; modulation amplitude, 1.0 G; number of scans ranged from 8 to 16 to obtain good signal-to-noise ratios.

Table S6 Spin Hamiltonian parameters of **1**−**4** and correlation times (τ_{corr}) in CH_3CN, THF, and toluene at room temperature (ca. 290 K). The standard errors for these parameters were not determined.

CH_3CN:

Complex	**1**	**2**	**3**	**4**
g_x	2.027	2.005	2.004	1.996
g_y	1.891	1.891	1.893	1.895
g_z	1.931	1.950	1.948	1.954
A_x (MHz)	223	242	235	243
A_y (MHz)	326	331	351	352
A_z (MHz)	122	100	90	88
τ_{corr} (ps)	150	187	211	257

THF:

Complex	**1**	**2**	**3**	**4**
g_x	2.028	1.994	1.991	1.988
g_y	1.886	1.900	1.894	1.892
g_z	1.943	1.960	1.963	1.963
A_x (MHz)	234	249	256	277
A_y (MHz)	351	350	380	352
A_z (MHz)	89	84	60	85
τ_{corr} (ps)	135	237	227	348

Toluene:

Complex	**1**	**2**	**3**	**4**
g_x	–[a]	1.974	1.978	1.987
g_y	–[a]	1.913	1.909	1.895
g_z	–[a]	1.967	1.964	1.956
A_x (MHz)	–[a]	267	262	270
A_y (MHz)	–[a]	315	340	352
A_z (MHz)	–[a]	106	101	109
τ_{corr} (ps)	–[a]	432	438	464

[a] **1** is insoluble in toluene.

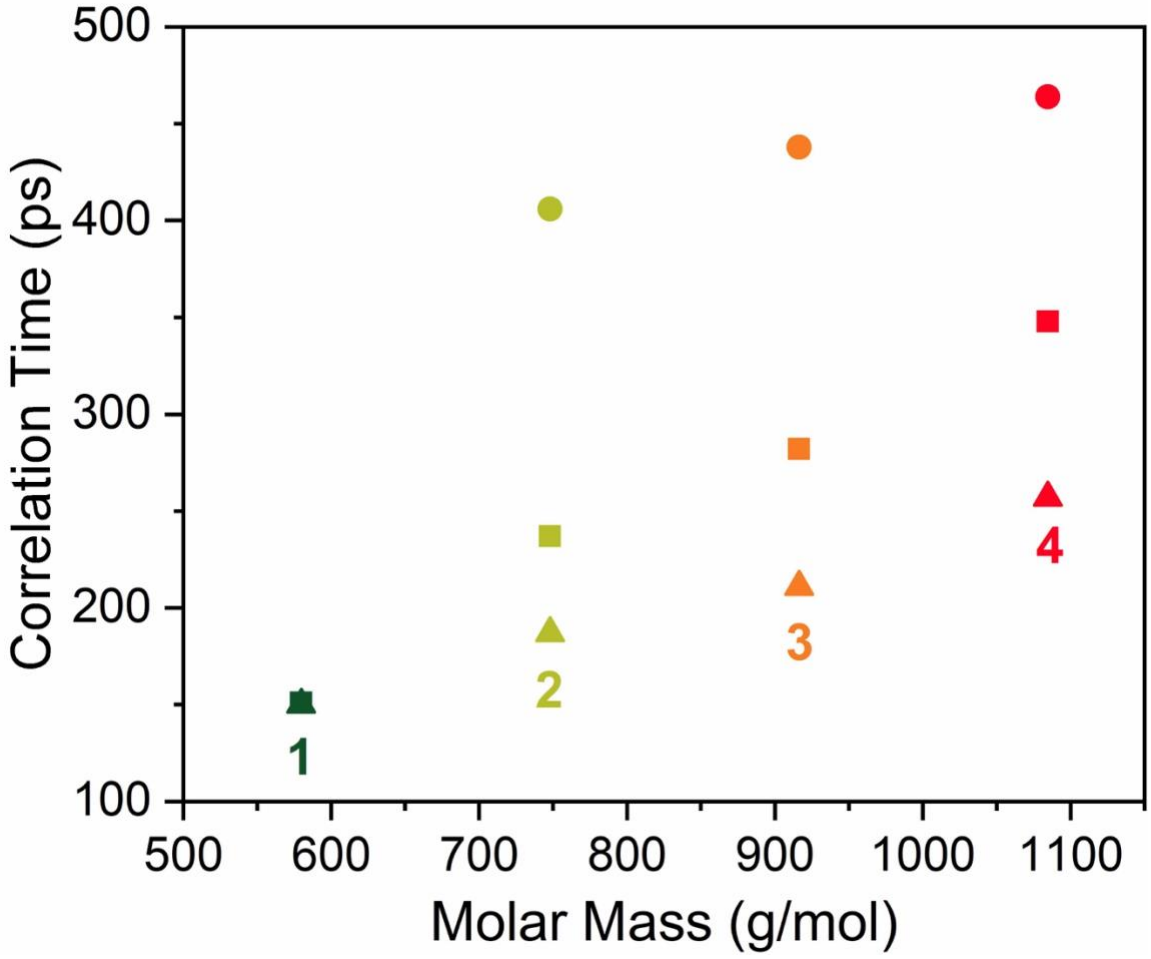

Fig. S9 A summary plot of correlation time of **1**−**4** in CH_3CN (▲), THF (■), and toluene (●).

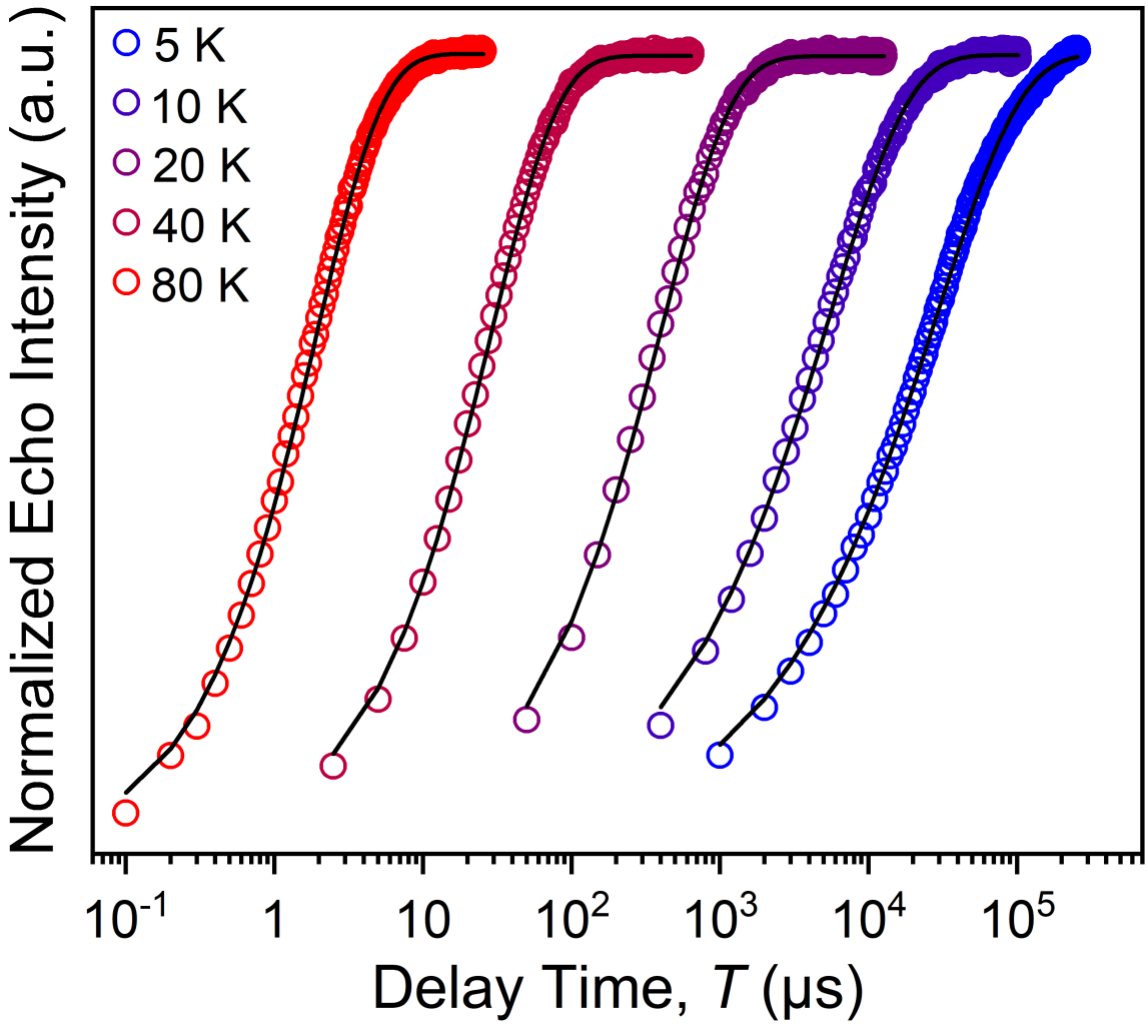

Fig. S10 Selected variable temperature inversion recovery curves (color traces) and fits (black traces) for **2**.

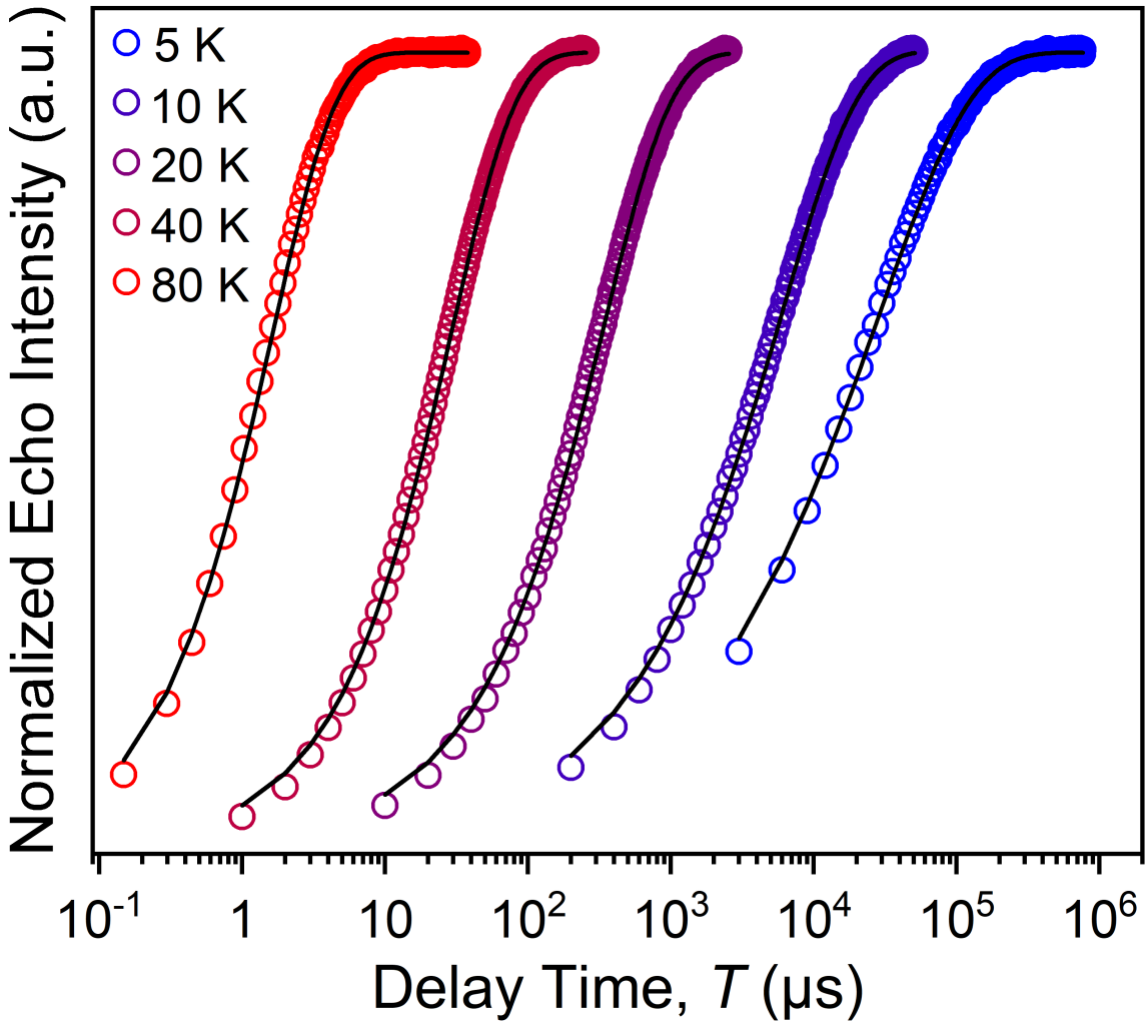

Fig. S11 Selected variable temperature inversion recovery curves (color traces) and fits (black traces) for **3**.

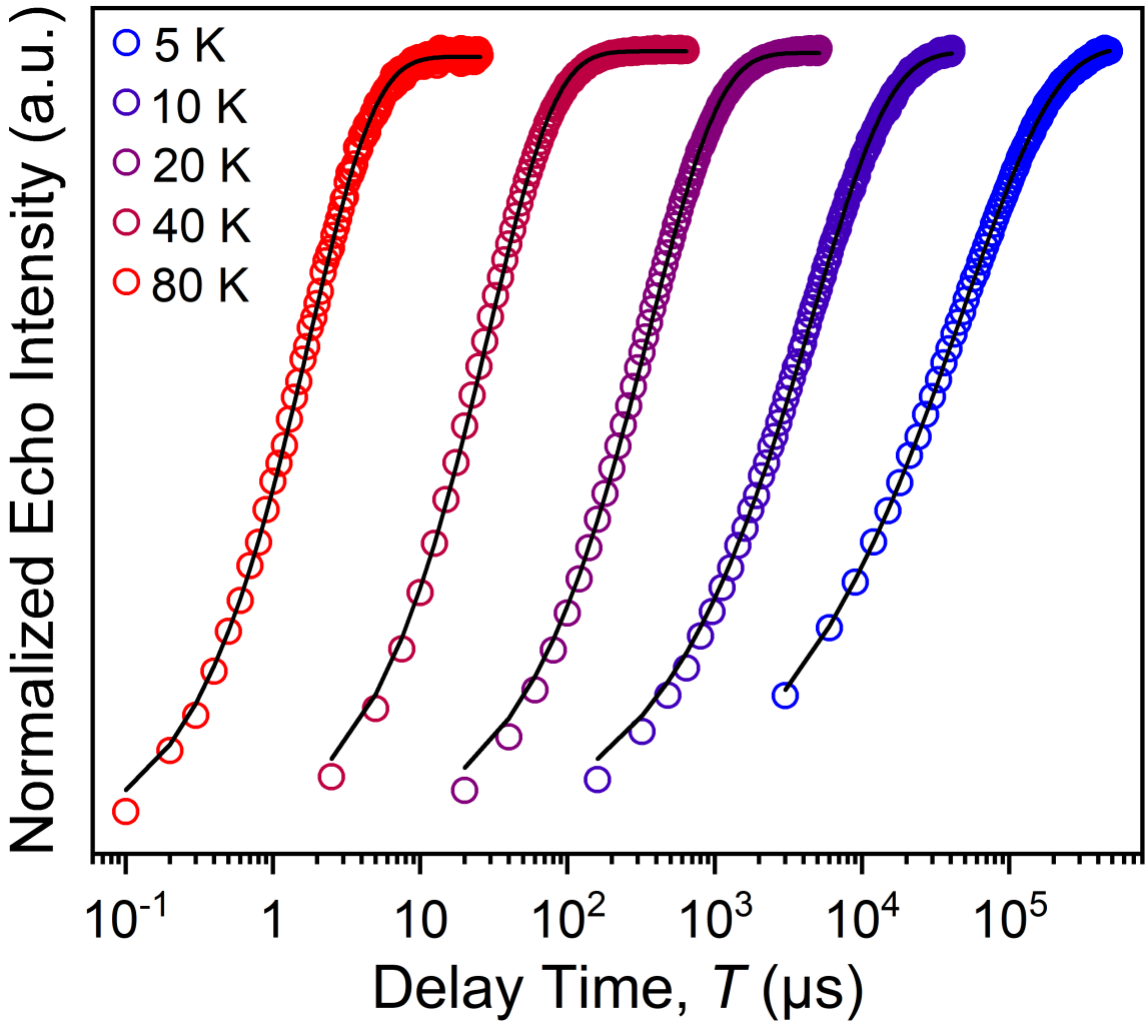

Fig. S12 Selected variable temperature inversion recovery curves (color traces) and fits (black traces) for **4**.

Table S7 Fit T_1 values from the fitting function $\mathrm{I}(t) = -A\left[e^{-\left(\frac{t}{T_1}+\sqrt{\frac{t}{q}}\right)} - \mathrm{I}(0) - 1\right]$. The standard error for each fit is reported in parentheses.

1:

T (K)	5	7	10	15	20	30
T_1 (μs)	148000(3000)	38000(1000)	8400(200)	3270(40)	432(5)	92(1)
q	0.0439(7)	0.0166(7)	0.0128(5)	0.0063(2)	0.0018(1)	$8.5(7)\times10^{-4}$
T (K)	40	50	60	70	80	90
T_1 (μs)	32.1(3)	14.3(2)	7.0(1)	3.68(5)	1.46(2)	1.56(6)
q	$4.4(4)\times10^{-4}$	$2.3(3)\times10^{-4}$	$1.3(2)\times10^{-4}$	$9(1)\times10^{-5}$	$5(1)\times10^{-5}$	$4(2)\times10^{-2}$
T (K)	100	110	130	140		
T_1 (μs)	1.13(2)	0.73(3)	0.58(6)	0.72(2)		
q	$2.2(2)\times10^{-5}$	$1.3(6)\times10^{-5}$	$1.3(6)\times10^{-5}$	$1(1)\times10^{-6}$		

2:

T (K)	5	7	10	15	20	30
T_1 (μs)	71000(2000)	49200(900)	10800(200)	1830(20)	532(7)	136(3)
q	0.057(2)	0.046(1)	0.0145(5)	0.0076(5)	0.0040(3)	0.0013(2)
T (K)	40	50	60	70	80	90
T_1 (μs)	33.7(3)	14.1(1)	8.70(7)	3.93(4)	2.13(2)	1.56(1)
q	$7.0(7)\times10^{-4}$	$3.2(3)\times10^{-4}$	$3.4(4)\times10^{-4}$	$1.2(2)\times10^{-4}$	$9.1(8)\times10^{-5}$	$7(1)\times10^{-5}$
T (K)	100	110	120	130	140	160
T_1 (μs)	1.218(9)	0.839(9)	0.68(1)	0.48(2)	0.40(2)	0.30(4)
q	$5.6(5)\times10^{-5}$	$3.1(4)\times10^{-5}$	$2.9(8)\times10^{-5}$	$1.4(6)\times10^{-5}$	$2(1)\times10^{-5}$	$2(7)\times10^{-5}$

3:

T (K)	5	7	10	15	20	30
T_1 (μs)	132000(3000)	37800(900)	12100(100)	2940(30)	447(4)	98.6(8)
q	0.0355(6)	0.0244(8)	0.0155(2)	0.0092(3)	0.0034(2)	0.0016(1)
T (K)	40	50	60	70	80	90
T_1 (μs)	33.1(3)	13.8(1)	6.72(5)	3.59(3)	1.79(1)	1.62(1)
q	0.0010(1)	$5.3(6)\times10^{-4}$	$3.1(4)\times10^{-4}$	$1.3(2)\times10^{-4}$	$8(1)\times10^{-5}$	$1.2(2)\times10^{-4}$
T (K)	100	110	120	130	150	170
T_1 (μs)	1.26(1)	0.911(7)	0.68(1)	0.56(1)	0.43(1)	0.20(3)
β	$1.0(2)\times10^{-4}$	$8(1)\times10^{-5}$	$8(4)\times10^{-5}$	$5.6(1)\times10^{-7}$	$4.3(1)\times10^{-7}$	$2.0(3)\times10^{-7}$

4:

T (K)	5	7	10	15	20	30
T_1 (μs)	178000(2000)	50000(800)	8600(100)	1620(20)	475(5)	98(1)
q	0.0676(7)	0.0247(5)	0.0139(5)	0.0051(3)	0.0040(3)	0.0020(2)
T (K)	40	50	60	70	80	90
T_1 (μs)	33.3(3)	13.6(1)	6.75(5)	3.54(3)	1.96(2)	1.85(2)
q	$9(1)\times10^{-4}$	$6(1)\times10^{-4}$	$4.0(4)\times10^{-4}$	$2.2(2)\times10^{-4}$	$1.0(2)\times10^{-4}$	$6(1)\times10^{-5}$
T (K)	100	110	120	130	140	160
T_1 (μs)	1.23(2)	0.95(1)	0.71(2)	0.57(2)	0.42(3)	0.30(5)
q	$5(1)\times10^{-5}$	$3.0(4)\times10^{-5}$	$7(4)\times10^{-5}$	$2(1)\times10^{-5}$	$2(2)\times10^{-5}$	–

Table S8 Fit parameters for the temperature dependence of T_1; see "EPR measurements" section for fitting equation. The standard error for each fit is reported in parentheses.

	1−4
A_{dir} ($K^{-1}s^{-1}$)	3.2(2)
A_{Ram} (s^{-1})	$1.8(1)\times10^{6}$
A_{loc} (s^{-1})	$5.0(1)\times10^{7}$
θ_D (K)	95(5)
Δ_{loc} (K)	440(10)

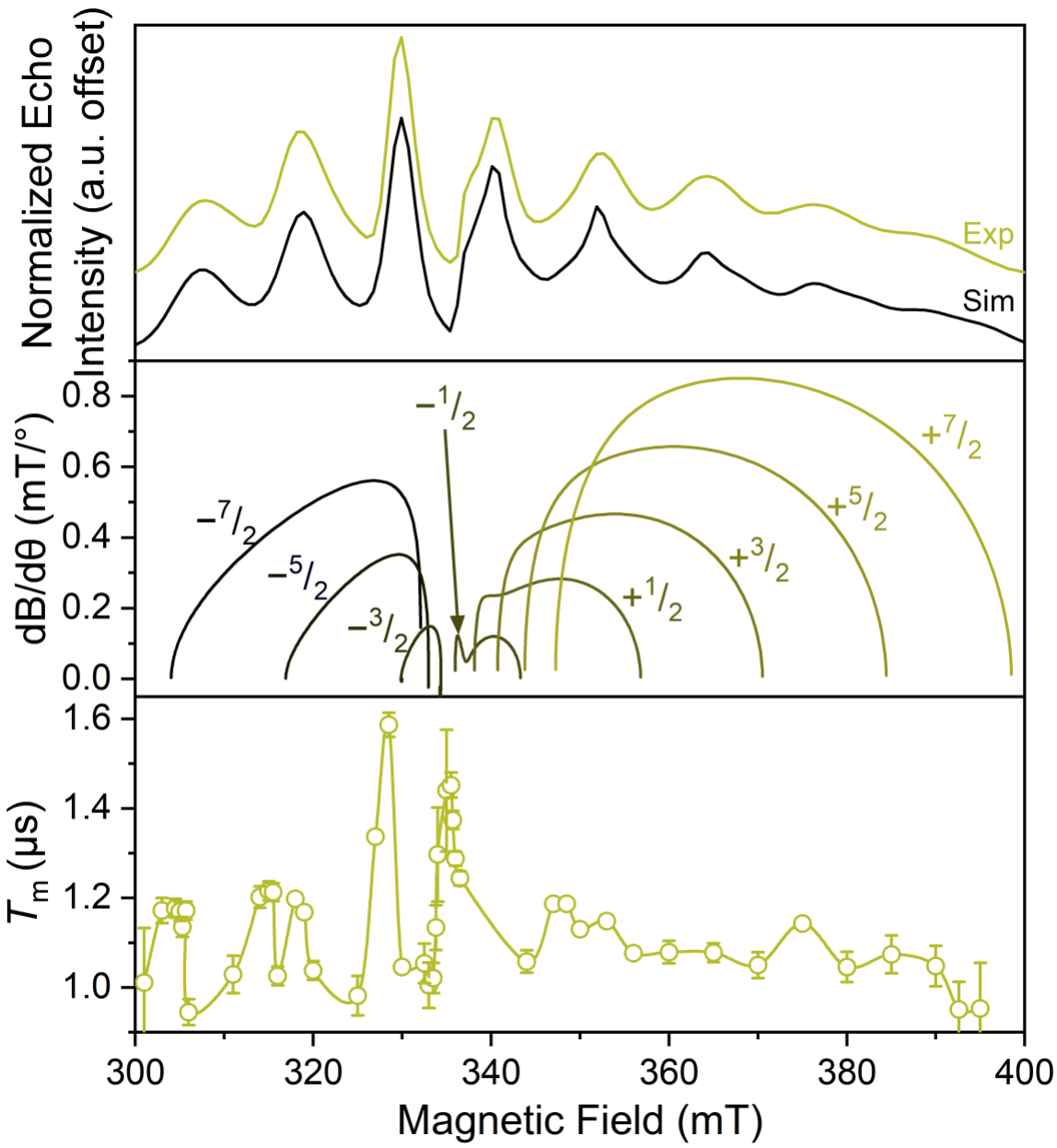

Fig. S13 (Top) X-Band (9.440 GHz) echo-detected, field-swept spectra of 1 mM **2** in *o*-terphenyl solutions at 5 K and simulations. (Middle) Derivative of the resonant field versus orientation for each of the transitions in the EDFS of **2**. Resonant field energies and derivatives were calculated from a simulation the of EDFS using microwave frequency = 9.444 GHz, *g*- and *A*-parameters listed in Table S4. (Bottom) Orientation dependence plot of **2** at 80 K. Error bars are not shown when smaller than the data symbols for clarity. The color trace is a guide to the eye.

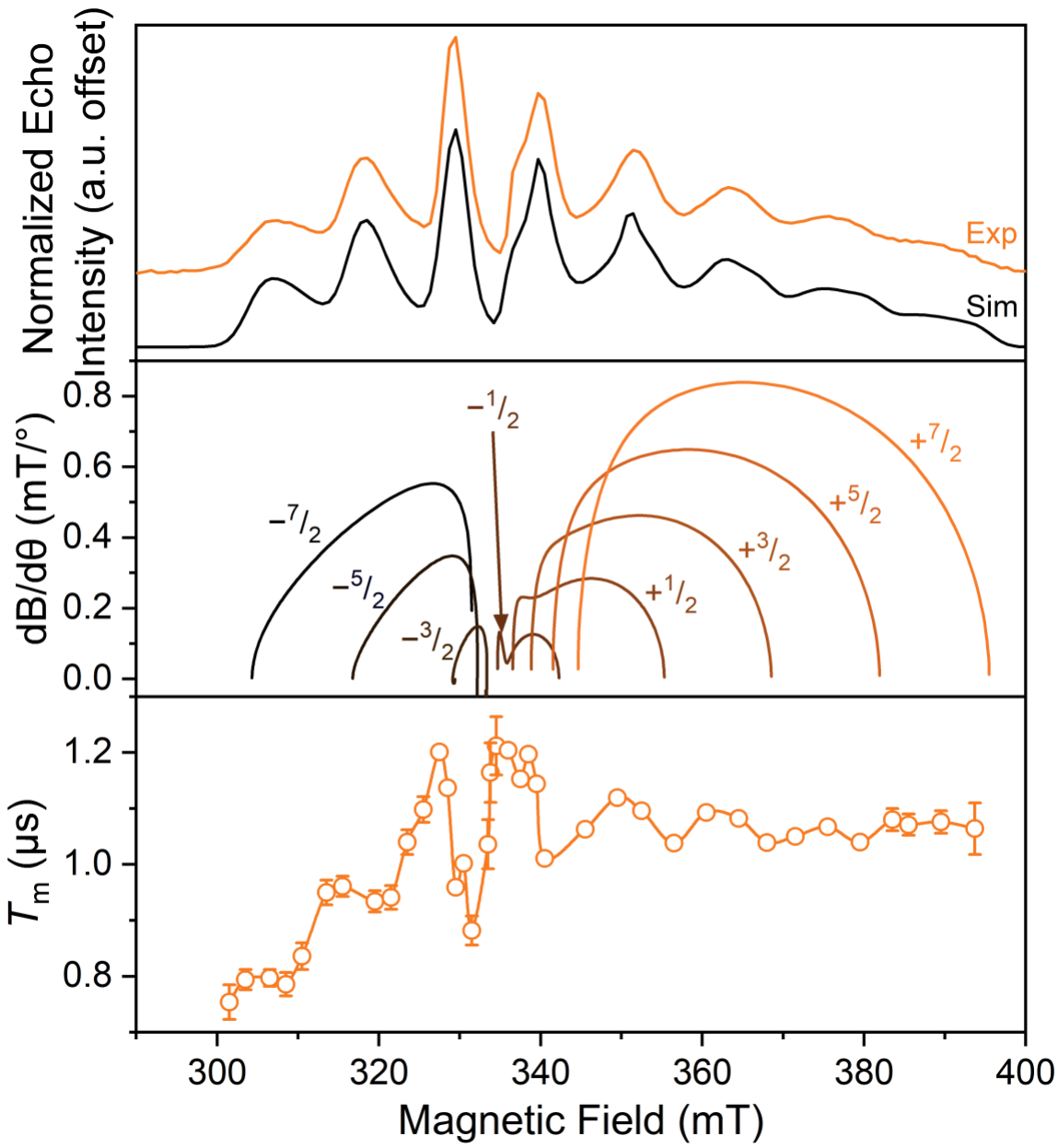

Fig. S14 (Top) X-Band (9.381 GHz) echo-detected, field-swept spectra of 1 mM **3** in *o*-terphenyl solutions at 5 K and simulations. (Middle) Derivative of the resonant field (here, B) with respect to orientation as a function of field for each of the transitions in the EDFS. The dB/dθ values were calculated using microwave frequency = 9.424 GHz (the measurement frequency of the bottom panel) and *g*- and *A*-parameters listed in Table S4. (Bottom) Orientation dependence plot of **3** at 80 K. Error bars are not shown when smaller than the data symbols for clarity. The orange trace is a guide to the eye. For better comparison across the panels, the 0.043 GHz frequency difference between the EDFS and T_m measurements was accounted for by a −1.6 mT shift in the bottom two panels. This value corresponds to the difference in resonant field for g = 2.00 at the two frequencies.

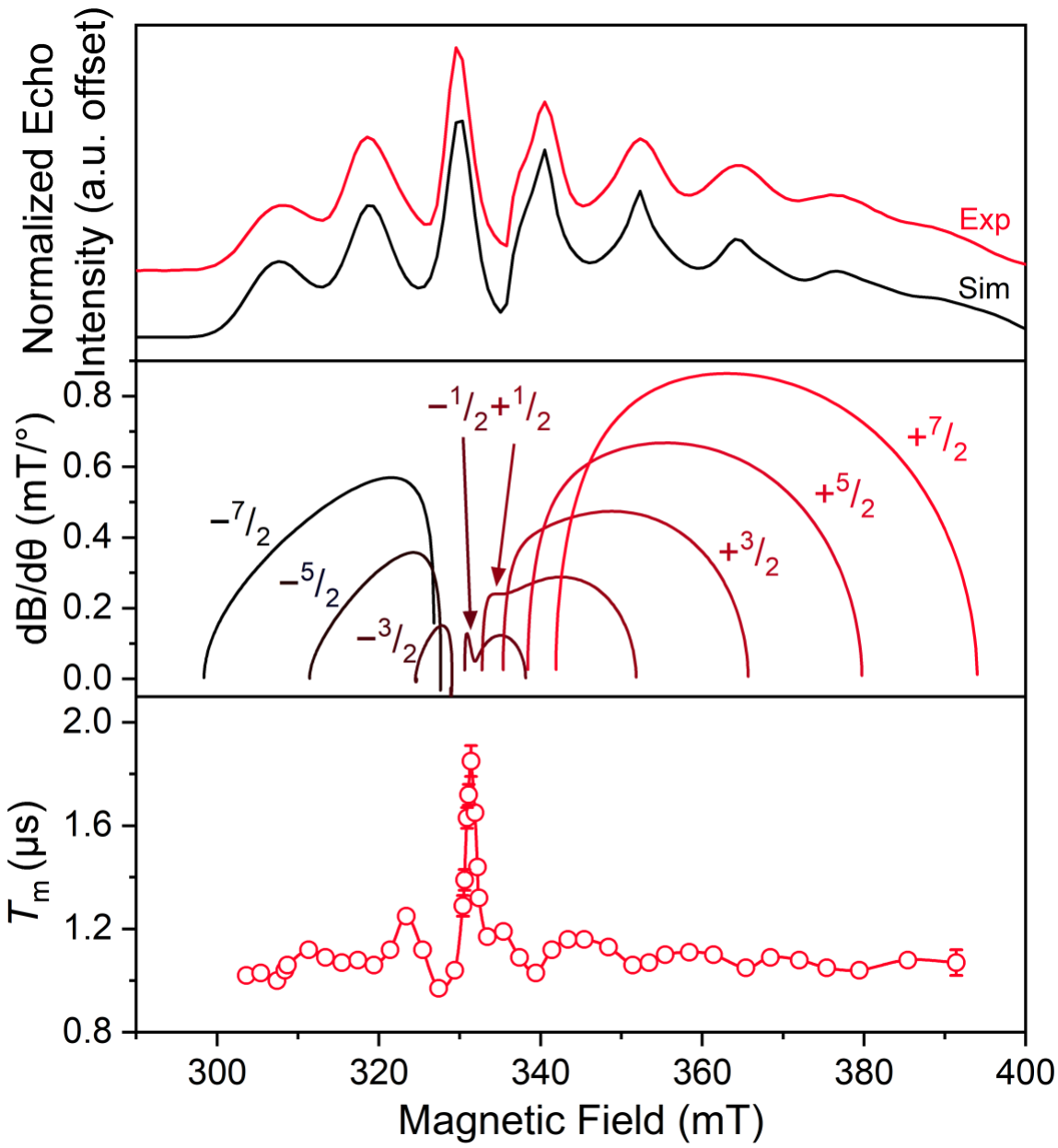

Fig. S15 (Top) X-Band (9.342 GHz) echo-detected, field-swept spectra of 1 mM **4** in o-terphenyl solutions at 5 K and simulations. (Middle) Derivative of the resonant field (here, B) with respect to orientation as a function of field for each of the transitions in the EDFS. The dB/dθ values were calculated using microwave frequency = 9.469 GHz (the measurement frequency of the bottom panel) and *g*- and *A*-parameters listed in Table S4. (Bottom) Orientation dependence plot of **4** at 80 K. Error bars are not shown when smaller than the data symbols for clarity. The green trace is a guide to the eye. For better comparison across the panels, the 0.127 GHz frequency difference between the EDFS and T_m measurement was accounted for by applying a −4.6 mT shift to the bottom two panels. This value corresponds to the difference in resonant field for g = 2.00 at the two frequencies.

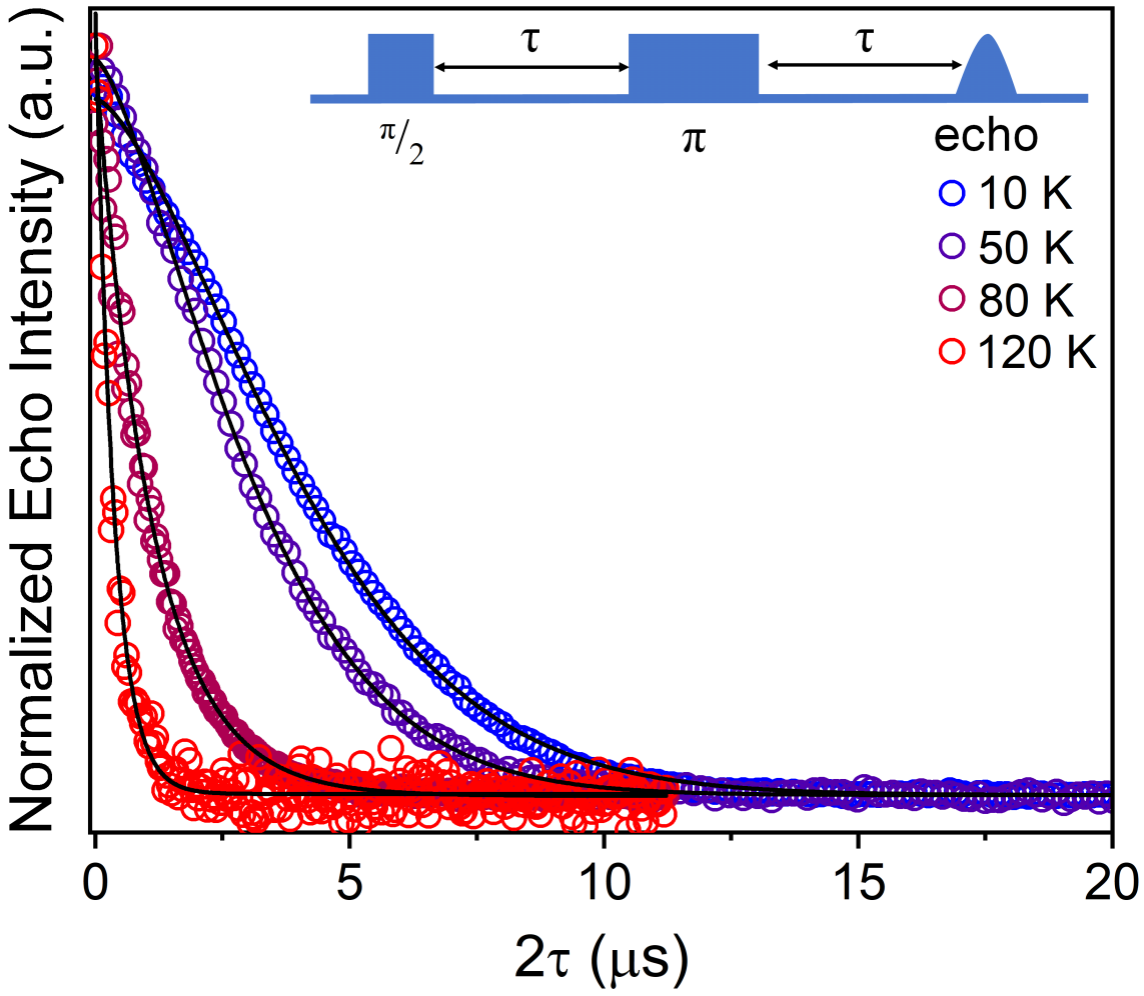

Fig. S16 Selected variable temperature Hahn echo decay curve (color traces) and fits (black traces) for **2**.

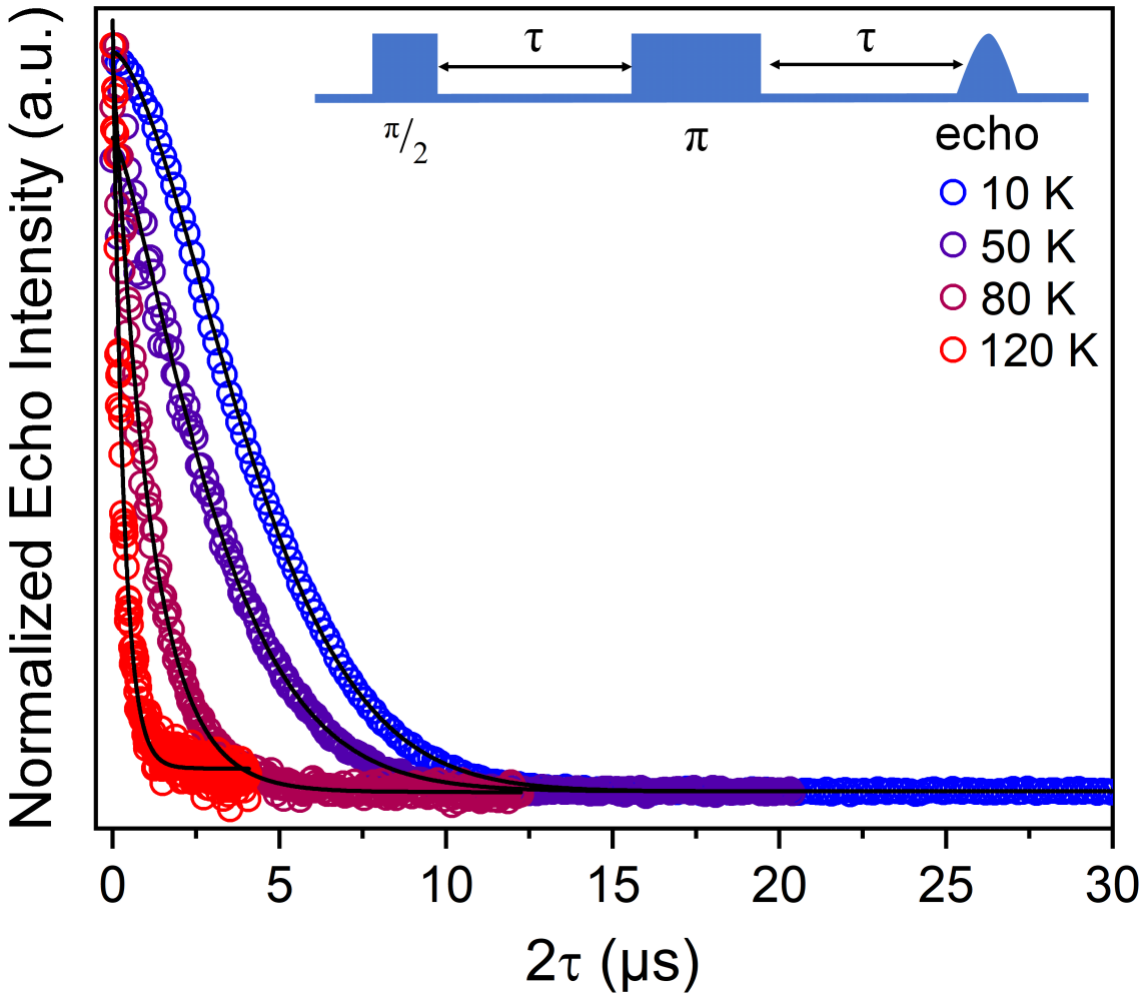

Fig. S17 Selected variable temperature Hahn echo decay curve (color traces) and fits (black traces) for **3**.

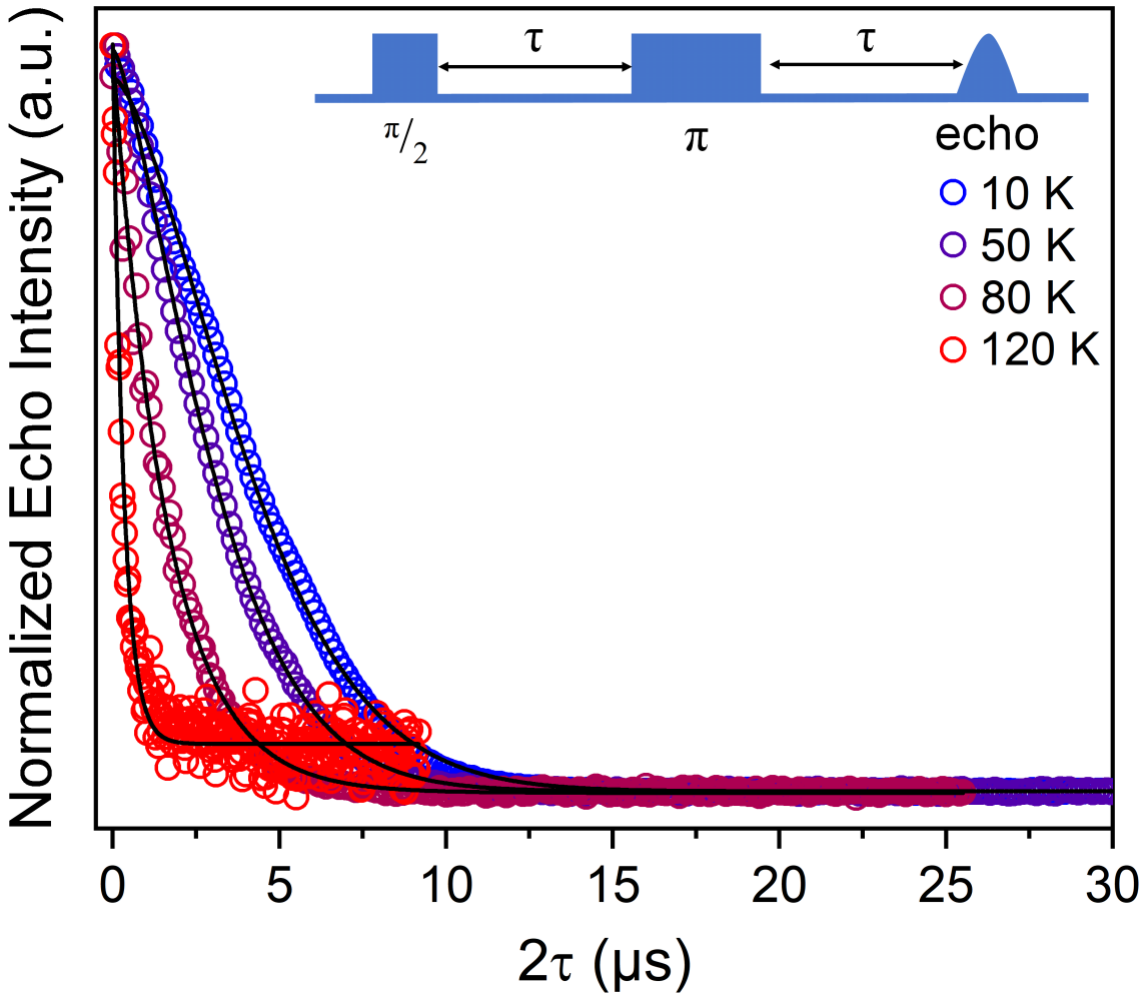

Fig. S18 Selected variable temperature Hahn echo decay curve (color traces) and fits (black traces) for **4**.

Table S9 Fit T_m values (in μs) and the stretch parameters (β) from the stretched exponential fitting function $I(2\tau) = I(0) - Ae^{\left(\frac{2\tau}{T_m}\right)^{\beta}}$. The standard error for each fit is reported in parentheses.

1:

T (K)	5	7	10	13	16	18	19
T_m(μs)	2.04(5)	2.08(5)	2.22(5)	2.46(5)	2.70(5)	3.05(5)	3.24(6)
β	0.69(1)	0.63(1)	0.72(1)	0.71(1)	0.74(1)	0.81(1)	0.84(1)
T (K)	22	24	30	32	36	41	46
T_m(μs)	3.18(5)	3.12(5)	2.91(4)	2.85(4)	2.64(4)	2.39(3)	2.05(2)
β	0.83(1)	0.83(1)	0.82(1)	0.82(1)	0.81(1)	0.797(9)	0.780(7)
T (K)	50	60	70	80	90	100	110
T_m(μs)	1.65(3)	1.15(1)	0.92(1)	0.770(9)	0.673(9)	0.526(8)	0.431(8)
β	0.75(1)	0.77(1)	0.89(1)	0.93(1)	0.93(1)	0.92(2)	0.94(2)
T (K)	120	140	160	180			
T_m(μs)	0.370(9)	0.26(1)	0.24(3)	0.15(5)			
β	0.96(3)	0.83(4)	0.87(9)	0.51(9)			

2:

T (K)	5	10	20	30	40	50
T_m(μs)	4.12(3)	4.67(2)	4.922(7)	4.708(6)	4.215(8)	3.46(1)
β	1.28(1)	1.51(1)	1.660(5)	1.671(5)	1.568(6)	1.433(7)
T (K)	60	70	80	90	100	110
T_m(μs)	2.598(9)	1.74(2)	1.14(1)	0.90(1)	0.628(9)	0.479(8)
β	1.297(7)	1.08(1)	1.03(1)	1.00(2)	0.98(2)	0.98(2)
T (K)	120	130	140	160		
T_m(μs)	0.36(1)	0.30(1)	0.24(2)	0.20(4)		
β	0.99(3)	0.98(5)	1.1(1)	1.4(6)		

3:

T (K)	5	10	20	30	40	50
T_m(μs)	4.42(2)	4.802(7)	4.870(8)	4.735(9)	4.06(3)	3.41(3)
β	1.43(1)	1.629(5)	1.678(6)	1.683(7)	1.44(2)	1.35(3)
T (K)	60	80	90	100	110	120
T_m(μs)	2.48(3)	1.13(1)	0.77(1)	0.55(1)	0.40(1)	0.318(8)
β	1.22(2)	1.02(2)	0.95(2)	0.94(2)	0.91(3)	0.98(2)
T (K)	130	140	157			
T_m(μs)	0.25(1)	0.221(8)	0.21(1)			
β	0.97(6)	1.31(8)	1.5(1)			

4:

T (K)	10	20	30	40	50	60
T_m(μs)	4.76(2)	4.89(1)	4.69(9)	4.185(9)	3.405(7)	2.49(2)
β	1.55(1)	1.660(8)	1.648(7)	1.547(6)	1.400(5)	1.20(2)
T (K)	70	80	90	100	110	120
T_m(μs)	1.66(2)	1.15(2)	0.79(1)	0.533(9)	0.400(9)	0.30(1)
β	1.05(2)	1.01(2)	0.98(2)	0.95(2)	0.95(2)	0.86(4)
T (K)	130	140				
T_m(μs)	0.27(3)	0.32(8)				
β	0.68(6)	0.50(7)				

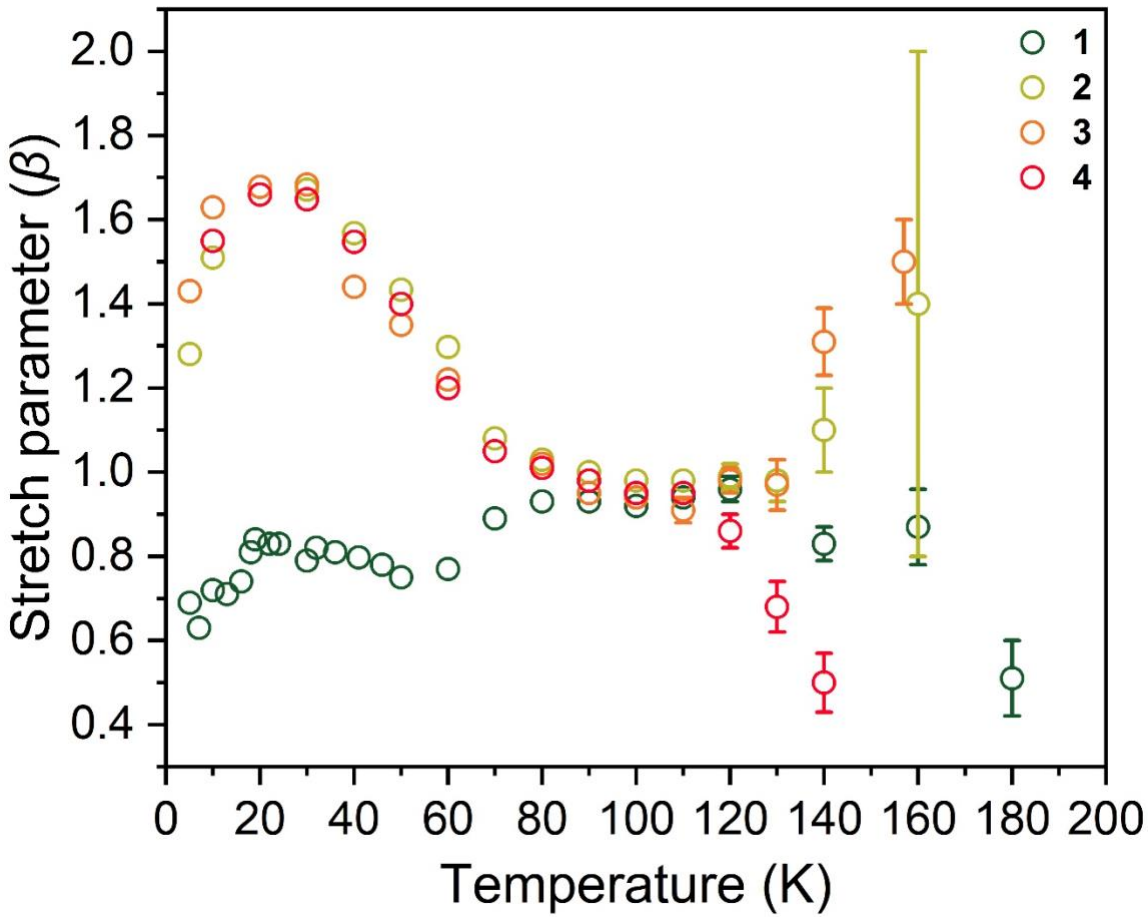

Fig. S19 Variable-temperature stretch parameters (β) plot. For clarity, error bars are not shown when smaller than the data symbols. The difference in the stretch parameter between **1** and **2**–**4** at low temperature is indicative of the impact of the methyl groups in the former on T_m.

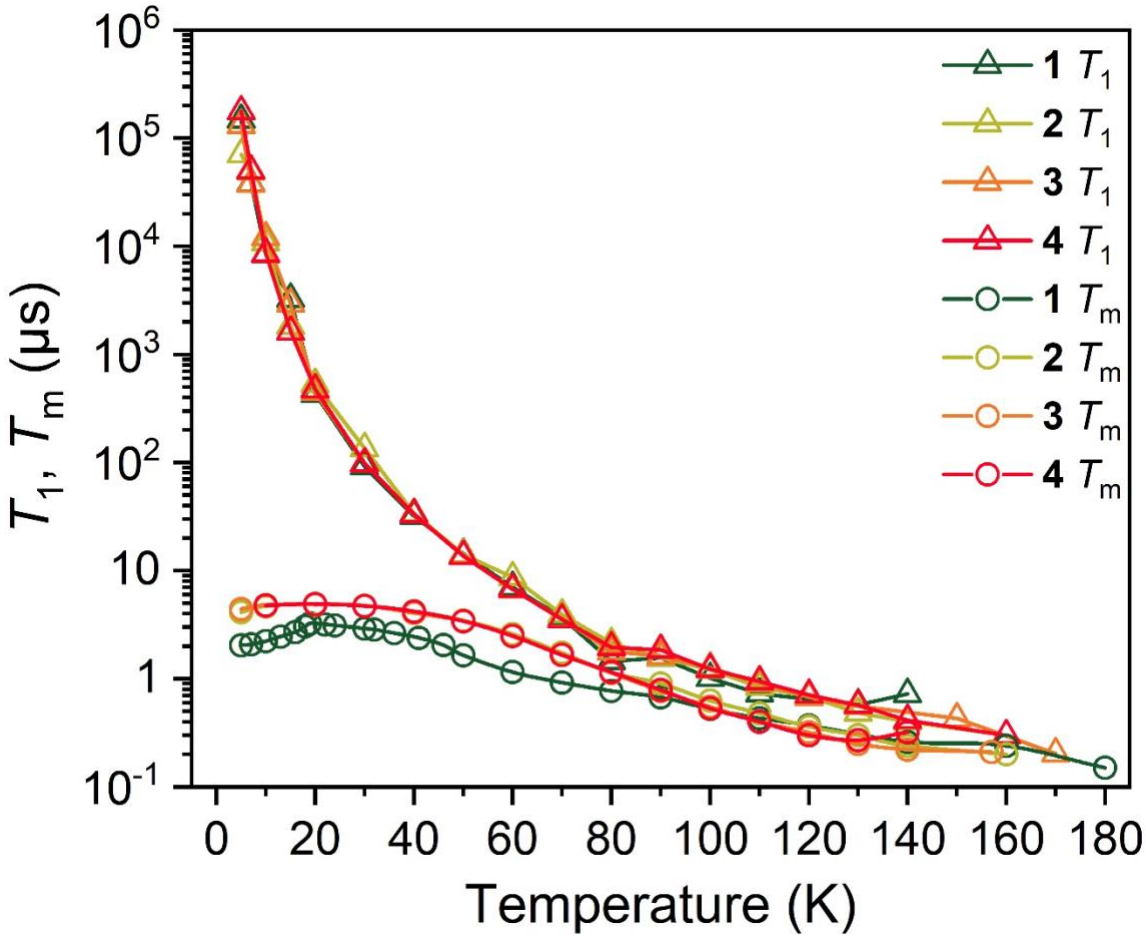

Fig. S20 Variable temperature T_1 and T_m plot for **1**−**4**. The color traces are guide to the eye.

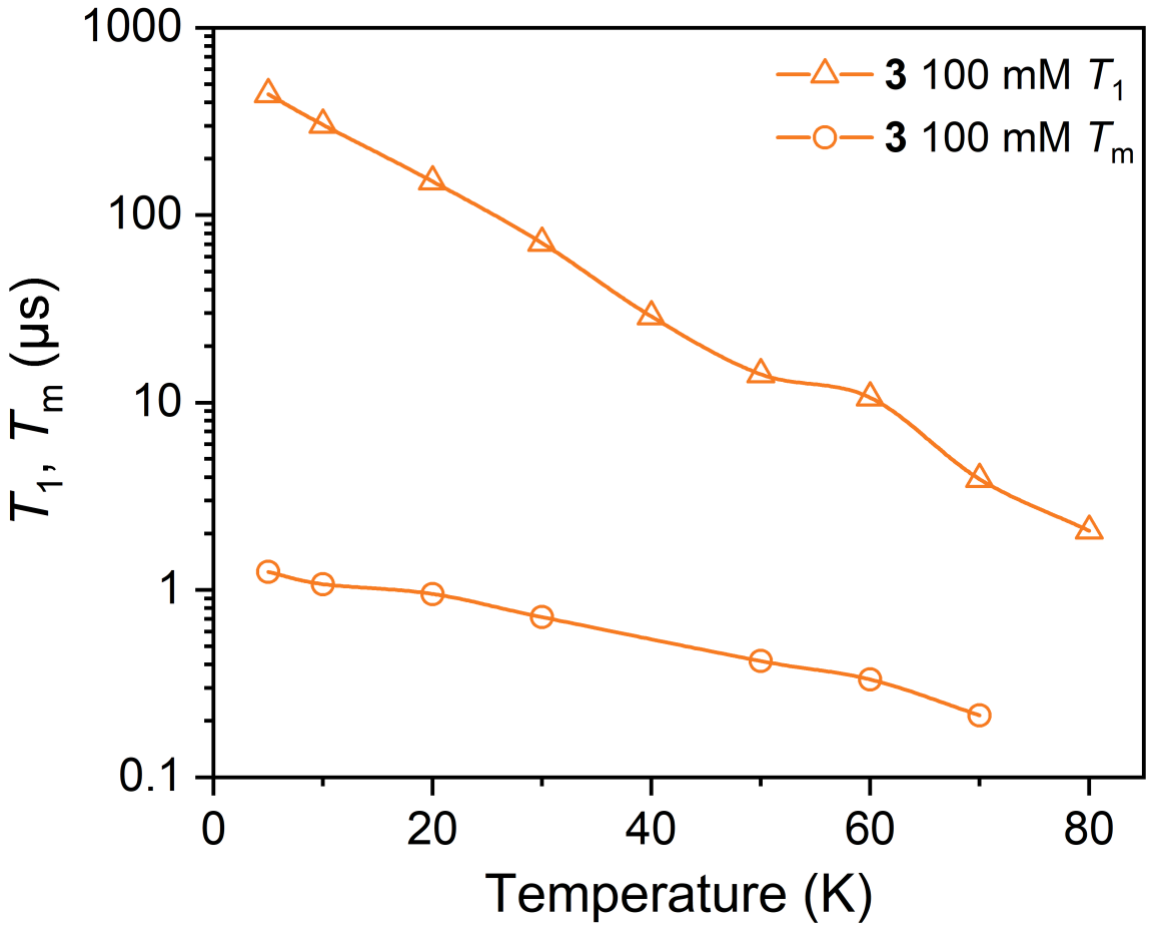

Fig. S21 Variable temperature T_1 and T_m plot for 100 mM **3** in *o*-terphenyl. The color traces are guide to the eye.

Table S10 Fit T_1 and T_m values (in μs) and the stretch parameter (β) from the stretched exponential fitting function for 100 mM **3** in *o*-terphenyl. See "Electron Paramagnetic Resonance" section for fitting function. The standard error for each fit is reported in parentheses.

T_1:

T (K)	5	10	20	30	40	50
T_1 (μs)	440(20)	300(30)	151(2)	71.1(6)	28.8(3)	14.2(2)
T (K)	60	70	80			
T_1 (μs)	10.6(6)	3.90(3)	2.07(7)			

T_m:

T (K)	5	10	20	30	50	60	70
T_m (μs)	1.248(9)	1.072(8)	0.952(8)	0.715(9)	0.417(6)	0.333(5)	0.214(4)
β	1.09(1)	1.31(2)	1.21(2)	1.09(2)	1.09(2)	1.18(3)	1.16(3)

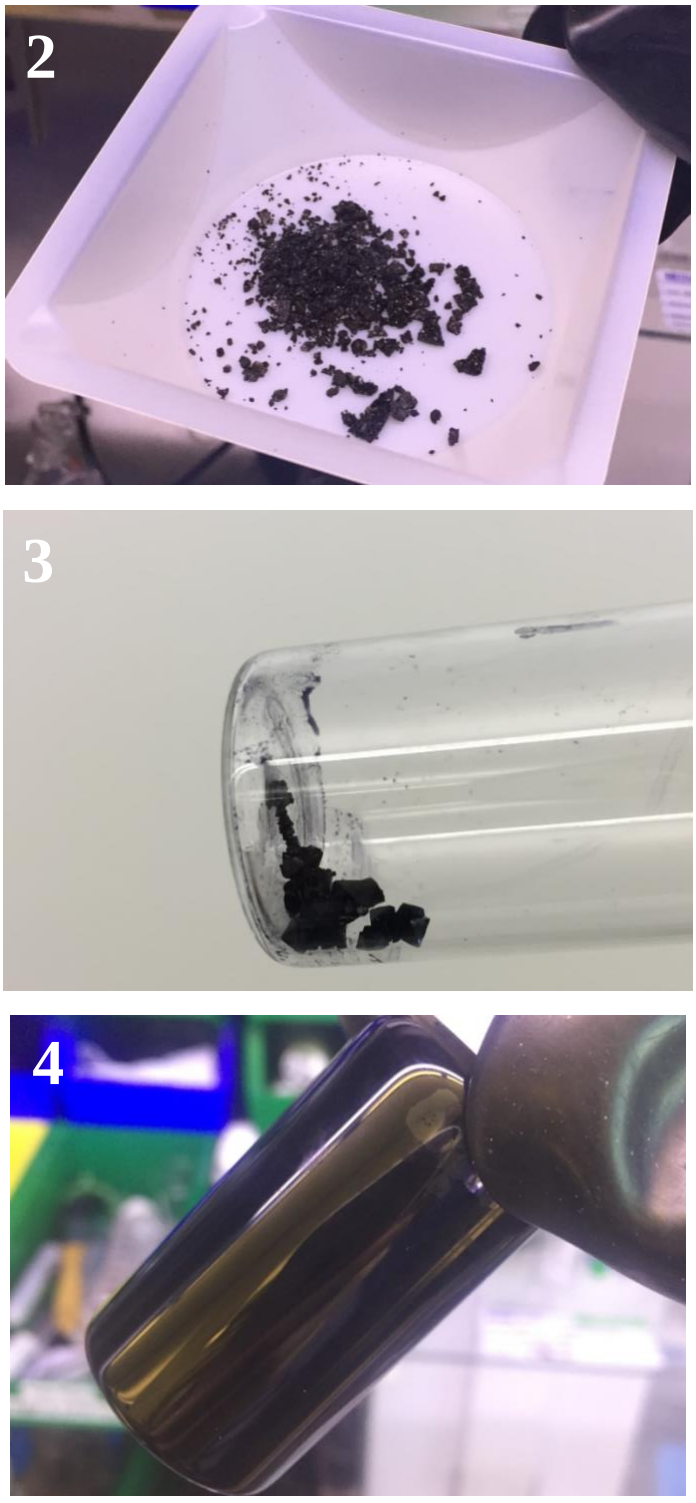

Fig. S22 Pictures of crystals **2** and **3** and highly viscous oil **4**.

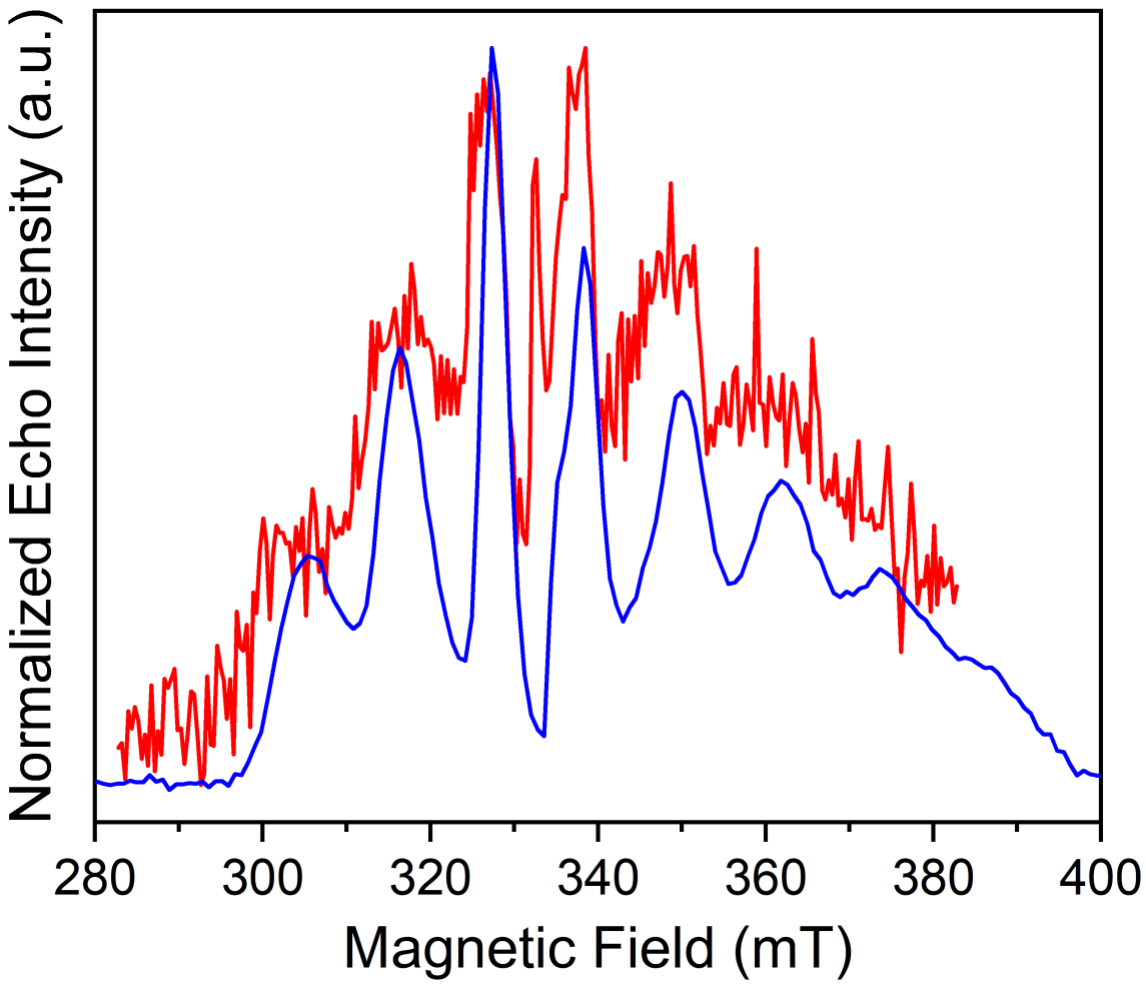

Fig. S23 Overlaid X-Band (red, 9.351 GHz; blue, 9.426 GHz) echo-detected, field-swept spectra of 1 mM **4** in frozen *o*-terphenyl at 80 K of a non-glass (red) and glass (blue) samples, illustrating the importance of glassing behavior in spectral quality. For better comparison, the 0.075 GHz frequency difference between these two measurements, was accounted for by a −2.7 mT shift in the 9.426 GHz measurement. This value corresponds to the difference in resonant field for g = 2.00 at the two frequencies.

Reference

1 S. R. Cooper, Y. B. Koh and K. N. Raymond, *J. Am. Chem. Soc.*, 1982, **104**, 5092–5102.

2 W. L. F. Armarego and C. L. L. Chai, *Purification of Laboratory Chemicals*, Elsevier, Oxford, 6th edn., 2009.

3 B. E. Bryant, W. C. Fernelius, D. H. Busch, R. C. Stoufer and W. Stratton, in *Inorganic Syntheses*, 1957, vol. 5, pp. 113–116.

4 C. Milsmann, A. Levina, H. H. Harris, G. J. Foran, P. Turner and P. A. Lay, *Inorg. Chem.*, 2006, **45**, 4743–4754.

5 G. M. Sheldrick, *SADABS*, Bruker Analytical X-Ray Systems, Inc., Madison, WI, 2000.

6 G. M. Sheldrick, *Acta Crystallogr. Sect. A Found. Crystallogr.*, 2015, **71**, 3–8.

7 G. M. Sheldrick, *Acta Crystallogr. Sect. C Struct. Chem.*, 2015, **71**, 3–8.

8 O. V. Dolomanov, L. J. Bourhis, R. J. Gildea, J. A. K. Howard and H. Puschmann, *J. Appl. Crystallogr.*, 2009, **42**, 339–341.

9 S. Stoll and A. Schweiger, *J. Magn. Reson.*, 2006, **178**, 42–55.

10 University of Denver EPR Center.

11 *Matlab*, The MathWorks Inc., Natick, MA, 2018.

12 *Origin*, OriginLab, Northampton, MA, 2018.

13 H. Chen, A. G. Maryasov, O. Y. Rogozhnikova, D. V. Trukhin, V. M. Tormyshev and M. K. Bowman, *Phys. Chem. Chem. Phys.*, 2016, **18**, 24954–24965.

14 T. J. Pearson, D. W. Laorenza, M. D. Krzyaniak, M. R. Wasielewski and D. E. Freedman, *Dalt. Trans.*, 2018, **47**, 11744–11748.

15 K. M. Salikhov and Y. D. Tsvetkov, in *Time Domain Electron Spin Resonance*, eds. L. Kevan and R. N. Schwartz, John Wiley, New York, 1979, pp. 232–277.

16 S. S. Eaton and G. R. Eaton, in *Biological Magnetic Resonance*, eds. L. J. Berliner, S. S. Eaton and G. R. Eaton, Kluwer academic/Plenum publishers, New York, 2002, pp. 29–154.

17 A. Schweiger and G. Jeschke, *Principles of Pulse Electron Paramagnetic Resonance*, Oxford University Press, Oxford, 2001.

18 J. Rumble, Ed., *CRC Handbook of Chemistry and Physics*, CRC Press, 99th edn., 2018.